QUANTIFYING THE SPATIAL MORPHOLOGY OF ORGANIC FILMS THROUGH POLARIZATION-DEPENDENT IMAGING

by

MADELYN N. SCOTT

A THESIS

Presented to the Department of Chemistry and Biochemistry,
the Department of Physics, and the Robert D. Clark Honors College
in partial fulfillment of the requirements for the degree of
Bachelor of Science

June 2020

An Abstract of the Thesis of

Madelyn N. Scott for the degree of Bachelor of Science
in the Department of Chemistry and Biochemistry and in the Department of Physics to be taken June 2020

Title: Quantifying the spatial morphology of organic films through polarization-dependent imaging

Approved: _____*Dr. Cathy Y. Wong*_____
Primary Thesis Advisor

Organic semiconducting materials are appealing, green alternatives to conventional semiconductors because they can be solution-processed into films. However, solution-processing fabrication methods can be prone to morphological disorder, which we define as the variety of sizes and shapes of crystalline structures produced within a single film. A large degree of morphological disorder in semiconducting films inhibits their electronic functionality for use in technological devices. Quantitatively characterizing the mesoscopic crystalline structures, or domains, of organic molecules after film formation from solution enables insight into how macroscopic deposition conditions, like temperature and solution concentration, affect spatial morphology.

We constructed a homebuilt microscope to acquire images of films with polarization-dependent transmission. To complement this technique, we also developed an image analysis software package to characterize film morphology. A series of images are collected at a single spatial location on the sample, rotating the polarizer

between each image. This process is repeated for several spatial locations on the film surface. For every pixel in the image, the absorption signal as a function of polarization angle is fit to a sinusoidal curve, and the parameters from the best-fit curves are used to create a panoramic image of the entire film surface. Once the panoramic image has been built, the sinusoidal fitting parameters are employed again to assign pixels in the image to discrete aggregate domains within the film. A collection of domain metrics (size and aspect ratio) are computed to describe the morphology of the film after these domain assignments have been made.

In this work, several organic films are produced under different deposition temperatures and solution concentrations. The resulting morphologies of these films are compared. This examination provides insight into how the physical properties of organic semiconducting films are affected by macroscopic differences in their formation environments. By better understanding the relationship between deposition conditions and film formation, existing solution-processing techniques can be further controlled and refined to achieve target physical properties in organic semiconducting materials.

Acknowledgements

I would like to thank my research advisors, Dr. Cathy Wong and Kelly Wilson, for their exceptional guidance and mentorship of my work. Even from the beginning of my time in the Wong Lab, Cathy and Kelly exercised strong investments in my future as a research scientist. They have fostered my technical skills, independence, and intellectual curiosity that will be crucial as I continue in my academic career.

During this project, I met frequently with Cathy and Kelly to troubleshoot solutions in my code, to develop clever techniques to test the accuracy of my computational results, and to keep me accountable for moving the research forward. Both Cathy and Kelly have provided me with a healthy balance of freedom to develop solutions on my own and hands-on involvement in my project. I am sincerely grateful to them for their support and encouragement in every step of my career thus far. I owe all of the incredible opportunities I have received—especially my acceptance to the Chemistry PhD program at MIT—in large part to Cathy and Kelly. It has been a pleasure getting to work with inspiring scientists who are also compassionate and thoughtful human beings.

I would also like to thank all of the wonderful people in my life who have supported me not only in my thesis, but also in completion of my undergraduate studies. My aunt, Pat, and my grandma, Helen, have shown me unwavering support throughout my entire life. I am incredibly grateful for their dedication and enthusiasm. They have taught me to follow my ambitions and to persevere even when challenges are ahead.

My brother, Griffin, has always been a source of encouragement for me. He always knows just what to say when I need a boost of motivation. I am so thankful to

have someone who can share in my background and that we can encourage each other in the pursuit of excellence.

To my father, Tom, I owe my passion for learning. From an early age, he passed on his sense of wonder for the world by taking me hiking, bringing me to science museums, and letting me help with his global art exchange. No idea is too big for him. My dad is also responsible for showing me that math and science can be fun. I am incredibly grateful to him for teaching me how to be curious about the world.

My friends, Brian, Dylan, and Jake have been a huge source of inspiration during my time at the University of Oregon (UO). Their friendship has been pivotal in surviving the day-to-day stress that comes with being a college student. We always push each other to excel and support each other in our research. It has been an honor sharing this undergraduate experience with them.

Lastly, I would like to thank all of my instructors and colleagues at UO who have challenged me to do my best. I am forever grateful for the opportunity to thrive amongst other scientists in the collaborative and supportive environment UO has to offer.

Table of Contents

List of Figures

Introduction: Transforming raw images into meaningful characterization metrics.

Framing the project.

My thesis is a continuation of the research I have conducted with my Primary Advisor, Dr. Cathy Wong, for the past three years. In the Wong Lab, we are interested in studying different molecular systems during structural formation. You can think of structural formation in molecular systems as analogous to putting a bunch of individual Lego pieces together to form larger objects. Systems in equilibrium (likened to a bunch of Legos spread on the floor, or the final Lego structure) have been extensively studied. However, we want to measure the electronic properties of these molecular systems *during* their structural formation (i.e. *as* the Legos are assembled!). Understanding these dynamic processes is vital in optimizing our industrial production of semiconducting materials for use in technologies, which include solar cells and electronic devices.

My project aims to characterize the sizes, shapes, and orientations of these molecular systems after their structural formation. I have built a research-grade microscope to image samples I have prepared under different environmental conditions. I have also developed an image analysis software package to extract meaning from these microscope images. Using these experimental and computational methods in tandem, I aim to characterize samples as a function of these environmental conditions. Ultimately, I want to connect the large-scale environmental conditions we can control (like temperature and solution concentration) to the tiny crystalline structures formed within the film. My thesis will present the background and theory necessary to

understand my work, the development and optimization of both the microscope and the computational software, as well as an extensive set of results to showcase the functionality of my experimental and computational tools.

Setting the stage for film characterization.

Organic semiconducting materials are versatile alternatives to conventional semiconductors because they can be solution-processed into films for use in electronic devices. However, solution-processing fabrication methods can be prone to morphological disorder[1,2]. We define morphological disorder as the variety of sizes and shapes exhibited by crystalline structures within a film. Semiconducting films with a high degree of morphological disorder tend to have limited electronic functionality and thereby less utility in devices[3]. This phenomenon occurs because the electronic properties of a film are dictated by the packing structure of and grain boundaries between the molecular aggregates which compose it[4].

One way to control the physical structure of a film is to perturb its deposition environment[5]. It follows that molecular aggregation events can be largely determined by the macroscopic conditions during deposition, like temperature and solution concentration[6,7]. In this work, we present a characterization strategy for quantifying film morphology and apply this technique to characterize films produced in several deposition environments. Quantifying how film morphology varies with different deposition

conditions enables insight into how the physical properties of organic semiconducting films can be controlled.

More control over the production of solution-processed films translates to increased reproducibility in their fabrication. By better understanding the relationship between deposition conditions and film formation, existing solution-processing techniques can be further refined to reproducibly achieve target physical properties in organic semiconducting films. Improving the reproducibility of solution-processing techniques will enable their widespread application in the manufacture of organic semiconducting films for use in technological devices—which can include solar cells, organic thin film transistors, and organic light-emitting diodes (OLEDs)[8–10].

How does a semiconductor work?

Many of the electrical components within technological devices are manufactured from semiconducting materials. A **semiconductor** is distinguished by its ability to conduct electrons only upon a thermal or optical excitation[11]. Unlike a **conductor**, electrons within a semiconducting material cannot flow freely unless an excitation is supplied by an external energy source.

Fig. 1 shows that in conductive materials, such as most metals, the energy spacing between the highest occupied molecular orbital (HOMO) and the lowest unoccupied molecular orbital (LUMO) is almost nonexistent. This energy spacing between the HOMO and LUMO is called the **band gap**[11]. When the band gap is small, electrons require very little external energy to reach the LUMO. A low energy barrier to overcome the band gap indicates that electrons can be easily conducted within the material[12].

In a semiconductor, the band gap is much larger than for a conductor (see Fig. 1). The energy structure of a semiconductor differs from that of conductive materials in the sense that the electrons are bound in the HOMO without any external excitation. However, as Fig. 1 shows, if enough energy is supplied to match the band gap, then

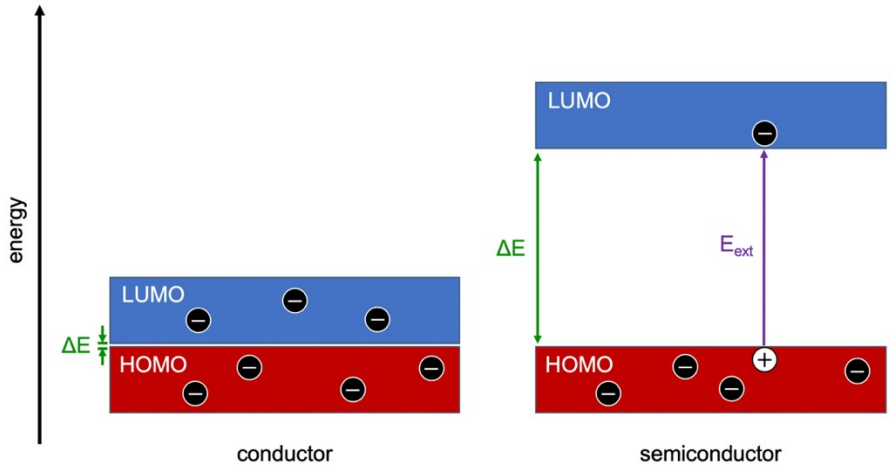

Fig. 1. Schematic representing the energy level diagrams of a conductor and of a semiconductor.

In a conductor, the band gap energy (ΔE) is very small, allowing electrons (black circles with minus signs) to flow freely within the material. In a semiconductor, the band gap is comparatively larger than for a conductor. An external energy source (E_{ext}) is necessary to excite an electron to the LUMO. Excitation of an electron to the LUMO leaves a hole (white circle with plus sign) in the HOMO. As more electron-hole pairs are generated, electron conduction can occur in the semiconductor material.

electrons can be conducted within the material. In other words, semiconductors can selectively conduct electrons in the presence of sufficient external energy.

Semiconductors have increased control over when conduction occurs because of their larger band gap energies. This property makes these materials extremely attractive for application in electronic devices, which require that the flow of electrons be controllable. Mainstream electronics conventionally employ silicon-based

semiconductors. As a semiconductor, silicon poses several advantageous qualities—it is an abundant, inexpensive resource; it can operate at high temperatures (300 K); and it can be easily doped with a complementary (electron-rich or vacancy-rich) material to improve electronic efficiency[13].

Why use organic semiconductors?

Another class of semiconducting materials are **organic semiconductors**. These materials are typically molecules with conjugated π-systems, which enables electrons to delocalize within the molecule[12]. Organic semiconductors possess an electronic structure that can also be described by Fig. 1. Just as in silicon-based materials, organic semiconductors require an external excitation source to initiate electron conduction.

There are several advantages to using organic semiconductors instead of silicon in electronic devices. One such advantage is the ability to tune the electronic structure of organic materials. During synthesis of organic semiconducting molecules, their structures can be customized to attain target electronic properties[14]. These properties can include narrow ranges of electronic absorption and emission energies. The ability to fine-tune the electronic properties of these materials enables their utility in optoelectronic devices, like OLEDs[15]. In other words, organic semiconductors enable the possibility of designer molecules for use in electronic devices.

In addition to their high degree of electronic tunability, organic semiconductors can be manufactured by solution-deposition[8]. Typically, most silicon-based semiconductors are prepared via physical vapor deposition (PVD) or chemical vapor deposition (CVD). In PVD, the material used to form the semiconductor is vaporized under vacuum, and eventually condenses onto a substrate to form a thin crystalline layer

of the semiconductor, called a film[16]. In CVD, the reaction between select chemical vapors deposits a new solid material, which becomes the film[17]. While effective in producing uniform films of the semiconductor, vapor deposition techniques are unideal due to the high quantities of material wasted during deposition. Since the materials used to form the films must be vaporized, only a small fraction of material actually forms the final film.

Most organic materials are currently produced using the same deposition techniques as for silicon. However, unlike silicon-based materials, organic semiconducting films can also be manufactured by various solution-deposition techniques. In **solution-deposition**, the process of film formation is analogous to how paint dries. The semiconducting material is dissolved in solution and deposited onto the substrate surface. As the solvent evaporates away, individual molecules aggregate together. The molecular aggregates form a solid film on the substrate surface after complete vaporization of the solvent. Film formation typically occurs within a few minutes, depending on the solvent and environmental conditions during deposition.

There are a variety of film deposition methods which utilize solution-processing. Some of these techniques include spin-coating, inkjet printing, and drop-casting[8]. Fig. 2 demonstrates the solution-deposition of a film via drop-casting. Film deposition by drop-casting is employed extensively in this work.

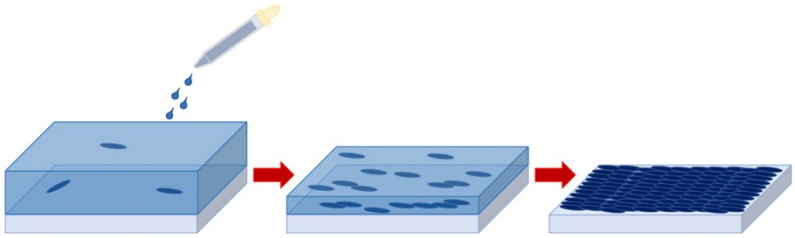

Fig. 2. Solution-deposition of an organic semiconducting film by drop-casting.

Solution containing the semiconducting molecule is deposited onto a substrate using a pipette (left). Aggregates are represented by the dark blue ovals. As the solvent evaporates (middle), more molecular aggregates form. After the solvent has completely evaporated (right), only a semiconducting film remains on the substrate surface.

Mimicking industrial-scale solution deposition.

Many organic semiconducting molecules are prime candidates for solution-deposition because they are highly soluble in inexpensive organic solvents. Solution-deposition is an ideal technique for industrial-scale film production because it minimizes waste and enables roll-to-roll printing strategies, thereby increasing manufacturing efficiency while decreasing the cost of production[10].

In this work, organic films are prepared in a two-step solution-deposition process. The first step is to prime the glass surface of the substrates with a wetting layer. The function of the wetting layer is similar to that of a paint primer. If a deposition solvent exhibits a high surface tension upon interaction with the substrate, it will not allow the solution to spread across the substrate surface[18]. A wetting layer primes the surface of the substrate by decreasing the surface tension of the solution and, consequently, weakening its cohesive forces[19]. By applying the wetting layer to the

substrate before depositing the molecule of interest, the surface coverage and the overall reproducibility of the films can be drastically improved.

The second step in film preparation is to drop-cast the molecule of interest on the primed substrate (see Fig. 2). This experimental approach was selected such that experimental techniques could be **scalable**. In other words, film preparation methods presented in this work are capable of being transferred to large-scale manufacturing processes. Choosing a scalable film preparation technique is critical in the application of small-scale experimental findings to large-scale, industrial film fabrication procedures.

Tuning mesoscopic structure through macroscopic perturbations.

While solution-deposition is a promising technique for minimizing wasted material during film production, it is not widely implemented due to its lack of reproducibility[1]. There can be many environmental factors that can alter the structural evolution of films from solution. These factors can include temperature, humidity, air flow, headspace, and solution concentration. Controlling for as many of these environmental factors as possible is essential to maximize the reproducibility of drop-cast films. Furthermore, understanding the relationship between macroscopic environmental perturbations and the resulting physical structure of the films produced is critical to improve and standardize solution-deposition techniques. These insights will also enable control over the structural morphology of the film.

Defining spatial heterogeneity.

The structural morphology of an organic film is intimately related to its electronic functionality. When two molecules aggregate, there is a change in electronic energy structure. This change depends on the transition dipole geometry between the two molecules[20]. Coulombic interactions between the transition dipole moments of two molecules can be thought of analogously to bar magnets. If two bar magnets are brought together with their positive ends in parallel, the magnets will repel. The overall state of this configuration is higher in energy than for an individual bar magnet. A similar energetic effect occurs for molecules with a "side-by-side" alignment of their transition dipole moments[20]. Conversely, when the opposite poles of two bar magnets are brought together, the magnets attract. When the magnets attract, the energy of the two-magnet system is lowered relative to the single-magnet system. Again, a similar effect can be observed in the electronic structure of two molecules aligned in a "head-to-tail" configuration[20].

It follows that the electronic structure of an organic film is dictated by physical structure of the molecular aggregates. As a result, the packing arrangement of molecules within the a crystalline film will determine its utility for electronic applications[21]. For this relationship between physical structure and electronic function to be exploited in the production of semiconducting films, it is necessary to quantify the degree of morphological disorder, or **spatial heterogeneity**, that is observed.

Fig. 3 contrasts two drop-cast films to demonstrate the range of spatial heterogeneity produced by this solution-deposition technique. As depicted in Fig. 3,

spatial heterogeneity can be identified by any structural defects, impurities, and grain boundaries within the film. These morphological features can inhibit charge transport[22].

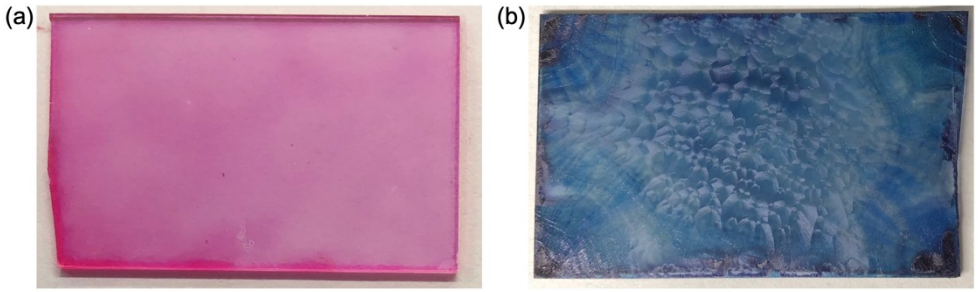

Fig. 3. Observing mesoscopic morphological disorder in drop-cast organic films.

A comparison between spatially (a) homogeneous and (b) heterogeneous films produced via solution-deposition. The spatially homogeneous film (pseudoisocyanine in acetone) does not exhibit any major grain boundaries or discrete domains within the film. Alternatively, the spatially heterogeneous film (TIPS-Pn in toluene) contains a high population of discrete crystalline domains.

Films should ideally be produced to minimize the spatial heterogeneity because an inhibition of charge transport translates to reduced functionality within an electronic device.

TIPS-Pn: a model system for characterizing spatial heterogeneity.

The molecule 6,13-bis-(triisopropylsilylethynyl) pentacene (TIPS-Pn) is not only an appealing organic semiconductor for electronic applications, but is also an ideal model system for characterizing spatial heterogeneity. As a solution of TIPS-Pn forms a structurally equilibrated film, individual aggregate domains can be observed on a mesoscopic scale. All crystalline domains in a structurally equilibrated film of TIPS-Pn have the same optical properties, which include absorption and fluorescence. However,

for a single polarization of incoming light, the optical response of the film depends on the orientations of the domains which exist there[23].

The relationship between optical response and physical orientation in TIPS-Pn structures can be explained through a consideration of the transition dipole moment (TDM). In classical electrodynamics, the electric dipole moment of an object describes its polarity, which can be thought of as its spatial distribution of positive and negative charges. This quantity is largely dictated by the geometric attributes of the object, which can include size, density, and shape[24]. The electric dipole moment is a useful measurement when considering the induced electric potential of an object, particularly after application of an external field.

In quantum mechanics, a quantity similar to the electric dipole moment emerges when considering how the electric field of a molecular structure interacts with an external electromagnetic field, like that from a light source. When a molecular system is exposed to an external electric field, its electrons can be excited between different electronic states. The probability that a particular electronic transition will occur (which is proportional to the measured absorption intensity) depends on its respective TDM. The TDM can be thought of as the electric dipole moment that describes the transition between a particular pair of electronic states. For example, the transition from the ground electronic state to the excited electronic state is only allowed if the TDM of the molecule can couple to the light. In other words, the direction of the TDM must overlap (at least in part) with the polarization of the external field for this transition to occur. The degree of overlap between the TDM of the molecule and the external field dictates the population of electrons which can undergo that particular electron transition[25].

Akin to the classical dipole moment, the TDM is directly correlated to the geometry of the molecule[20]. The relationship between the TDM and molecular geometry is the result of how charged particles are distributed throughout the molecule. For pentacene derivatives, including TIPS-Pn, the TDM from the ground electronic state to the first excited state exists along the short axis of the molecule (see Fig. 4)[20].

The connection between the TDM and molecular geometry enables the use of optical measurement techniques to determine the relative orientations of molecular structures within a larger bulk material[25,26]. For example, each mesoscopic crystalline domain within a TIPS-Pn film is comprised of a collection of molecular structures with TDMs oriented in the same direction[9]. As a result, an entire domain exhibits a uniform, polarization-dependent absorption intensity. This phenomenon is depicted schematically in Fig. 4.

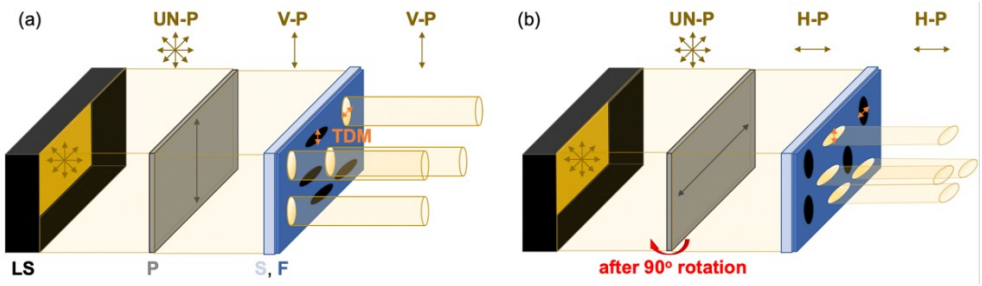

Fig. 4. Polarization-dependent transmission in TIPS-Pn films.

UN-P, unpolarized; V-P, vertically polarized; H-P, horizontally polarized; LS, light source; P, polarizer; S, substrate; F, film; TDM, transition dipole moment. Light propagates from left to right, originating from the light source. TIPS-Pn films (dark blue) exhibit a polarization-dependent coupling to the incoming light (yellow)[27]. Ideally, a polarizer (grey rectangle) only lets one orientation of light through. Domains are depicted by ovals along the film. Arrows above the light indicate the polarization. In (a), horizontal (*H*) domains transmit a maximal quantity of the incoming light, while vertical (*V*) domains transmit a minimal quantity of the incoming light. In this case, the TDM (orange arrow) of the *H* domains are decoupled to the incoming light and those for the *V* domains are coupled. (b) shows the same system after a 90° rotation of the polarizer. In this case, the TDM of the *V* domains are decoupled to the incoming light and those for the *H* domains are coupled.

Fig. 4 schematically demonstrates that solution-deposited TIPS-Pn films are comprised of distinct domains on the surface of the substrate. Each of these domains has its own TDM orientation, which dictates its optical response. These mesoscopic domains are evident in Fig. 3(b). As shown in Fig. 3(b), clear grain boundaries exist between these domains, making it easily to distinguish them by eye. An abundant population of large, distinct domains signify a high degree of spatial heterogeneity. Therefore, TIPS-Pn films are an ideal model system for the examination of spatial heterogeneity in organic films. Furthermore, films of TIPS-Pn can be produced with different degrees of spatial heterogeneity depending on the deposition conditions, like temperature and solution concentration. By changing these environmental parameters

during film deposition, the structural morphology of TIPS-Pn films can be controlled and characterized[23,28].

Using polarization-dependent brightfield microscopy to image TIPS-Pn samples.

The structural morphology of TIPS-Pn films can be characterized by studying film absorption as a function of polarization angle. A spatially resolved data acquisition technique is necessary to connect absorption measurements to spatial heterogeneity within the film. Microscope imaging can be used to satisfy this constraint. In this work, we employ **brightfield microscopy**, in which contrast is created by dark sample features and a bright, well-illuminated background[29].

An introduction to brightfield microscopy.

Brightfield microscopy is the simplest form of optical microscopy because it does not require any specialized optomechanical elements. A brightfield microscope collects light from a light source, directs it to the sample with a series of lenses, and records information about the sample features (stored in the light) using a detector.

The optical path of a brightfield microscope starts at the light source. In brightfield microscopy, this light source is typically broadband, meaning that several wavelengths are output simultaneously. Next in the path is the collector lens. This lens directs light from the light source into the optical path of the sample. This lens is necessary because undirected light (emitted by the light source) does not have enough intensity to show signal in measurements by the camera. After the collector lens is the condenser lens, which focuses light in the optical path onto a localized spot on the sample. The focal length of the condenser lens will determine the how much of the

sample is evenly illuminated. Ideally, the size of the illumination spot should be greater than the field of view imaged by the camera.

The two most important lenses in a brightfield microscope are the **objective lens** and the **tube lens**. The function of the objective lens is to collect light after propagation through the sample. The tube lens collects incoming light from the objective lens and focuses it onto the pixel array of the camera detector. The ratio of focal lengths between the objective lens and tube lens will determine the magnification of the image. The magnification, *M*, can be expressed as,

$$M = \frac{f_{tube}}{f_{obj}}, \tag{1}$$

where f_{tube} is the focal length of the tube lens, and f_{obj} is the focal length of the objective lens. If f_{tube} and f_{obj} are equal, then no magnification is achieved.

Achieving Köhler illumination.

In order for a brightfield microscope to acquire accurate images of a sample, it must be aligned such that all features of the light source are defocused at the sample plane. If not completely defocused, the light source can introduce artificial glare and shadowing into the image of the sample. These artifacts, which are caused by uneven intensity present in the light source, inhibit accurate measurement of the sample. One alignment strategy, called **Köhler illumination**, can be performed to defocus the light source at the sample plane.

The process of Köhler illumination can be understood by first considering how light propagates through a lens. When a lens is placed a single focal length after object (in the optical path), the spatial features of the object are mapped to the frequency

components of the transmitted light. In other words, the lens masks the spatial information contained in the light one focal length after the object. In *4f* imaging, spatial information is regained four focal lengths away from the object. Fig. 5 illustrates this concept through ray tracing. In a brightfield microscope, Köhler illumination is achieved by manipulating this property of lenses to ensure that there are no features of the light source at the plane of the sample. Light that is completely defocused at the sample plane ensures that only features of the sample are measured in the transmission images collected by the camera.

Introducing a polarizer to a brightfield microscope.

In this work, we present a brightfield microscope modified to acquire polarization-dependent transmission images. Given that TIPS-Pn exhibits polarization-dependent transmission, this feature can be exploited to characterize mesoscopic spatial heterogeneity[26]. To characterize film morphology using polarization-dependent

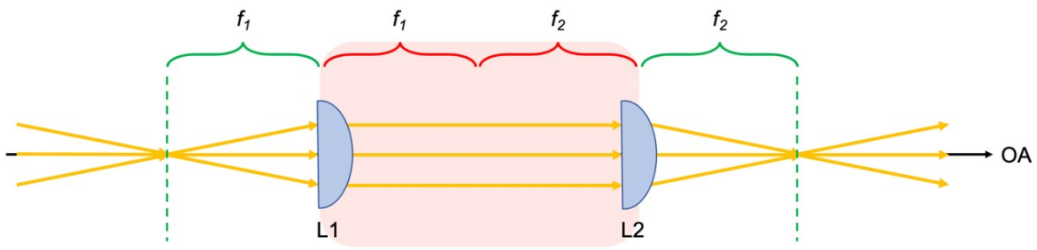

Fig. 5. Light propagation through a *4f* imaging system.

The object plane is indicated by the leftmost vertical green line. As light propagates through the lens, the spatial information of the object is completely defocused. The object is defocused through the red region. After passing through the second lens, the light begins to converge, and the spatial information describing the object is regained.

transmission, it is necessary that brightfield images are collected over a series of different polarization angles. A linear polarizer, secured to a motorized rotation mount, is introduced into the optical path of a homebuilt brightfield microscope. A rotating polarizer enables brightfield imaging at a series of polarization angles. These data can be used in a homebuilt image analysis software to quantify the degree of spatial heterogeneity in TIPS-Pn.

Employing sinusoidal fitting to extract physical meaning from microscope images.

Raw image files containing the polarization-dependent transmission at different spatial locations at the sample do not yield quantifiable determinations of spatial heterogeneity. Therefore, it is necessary to extract meaning out of these images by performing a series of computational routines. The first of these routines is convert the measured transmission signal to absorbance and fit these data pixel-by-pixel (as a function of polarization) to a sinusoidal waveform.

The utility of the sinusoidal waveform.

The periodicity of linear polarizers can be exploited to extract meaningful, quantitative information out of the raw transmission images. As a linear polarizer is rotated over a range of 180^{o}, we should expect there to be an angle value where light is maximal transmittance, and an angle value where light is minimally transmitted. These angle values can be defined as the maximum and minimum angles, respectively. Given that the transmission of the polarizer is bounded by a maximum and minimum angle, the oscillatory transmission pattern can be well described by a **sinusoidal function**. This class of functions provides an adequate set of models for periodic behavior. As a

result, the polarization-dependent transmission signal of the sample can be modelled well by a cosine function.

It is ideal to use a cosine function to model polarization-dependent transmission because cosine is well behaved and can be fit easily to three different parameters. These parameters include the **amplitude**, **phase shift**, and **vertical offset** of the sinusoid (see Fig. 6). The maximal amplitude describes the maximal output signal. The phase shift indicates how far from the "starting point" of the functional form the argument of the signal is. The vertical offset is a description of the baseline average for the signal. In other words, the vertical offset is the central value around which the function oscillates.

A physical interpretation of the phase shift parameter.

The amplitude, phase shift, and vertical offset of a sinusoid correspond to physically significant quantities. The amplitude, in the case of a film, describes the

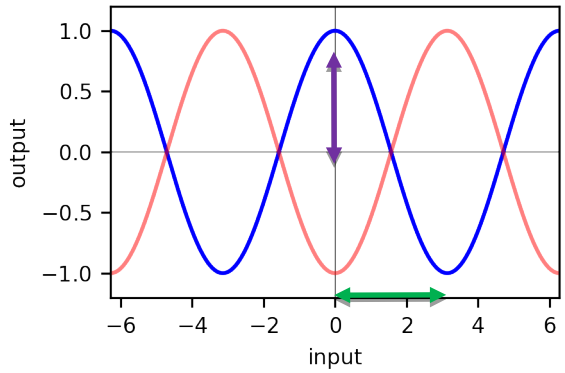

Fig. 6. Defining the characteristic parameters of sinusoidal functions.

The blue trace shows a cosine function, while the red trace shows a sine function. Cosine and sine differ by a phase shift (φ) of $\pi/2$, as shown by the green arrow. The maximal amplitude (purple arrow) describes the distance between the average value of the sinusoid and its maximal output. The vertical offset (not shown) describes the vertical shift necessary to return to an average value of zero.

range of optical densities over the surface of the film. Optical density is indicative of film thickness. For TIPS-Pn films, the phase shift can be a gauge of the relative orientations between crystalline domains. Finally, the vertical offset can be thought of as a measure of the average film thickness.

In the analysis of spatial heterogeneity presented in this work, the most relevant sinusoidal parameter is the phase shift. The phase shift can be connected to domain orientation by considering the mathematical interpretations of two destructively interfering sinusoids. An example can be observed in Fig. 6, where the relative phase shift between waveforms is $\pi/2$.For means of illustration, consider two distinct domains within a film, each with a distinct sinusoid describing its polarization-dependent transmission. The relative phase shift between these sinusoids demonstrates that the maximum angle occurs at a different angle position for each of these domains.

If the maximum angle differs between these domains, then the physical packing of the domains must be distinct. Different packing structures signal that the overall orientation of the two domains must be unique from one another, thus confirming that the two domains are also distinct.

Image stitching: Building a panorama shot.

To fully define and assess the differences between domains within a film, the entire surface of the film must be measured. However, the microscope instrument presented in this work is not capable of measuring the entire film in one image. The film area captured at a single spatial location on the film is small relative to the size of typical domain. To overcome this limitation, images are collected at several spatial locations on the film and are stitched together. This solution, in essence, creates a **panorama** image of the sample.

In a smartphone camera, for example, a panorama shot takes several images as the device is translated across the field of view and patches them together. “Seams” between different spatial locations are bound to occur with tilting of the device during translation. Often times these “seams” between individual images are smoothed out with a mathematical image mixing scheme. “Seam” smoothing occurs as the phone algorithm matches spatial coordinates of the two images according to their common features. Repeating this process for several images generates the full panorama image, capturing the full desired field of view.

A similar technique can be applied to the microscopy data, enabling the construction of panorama film images. As described above, a sinusoidal model and corresponding fits are generated for each pixel at a single spatial location on a film.

Each spatial location of a film can be represented by a unique amplitude, phase shift, and vertical offset maps, generated from the pixel-by-pixel fitting routine. Using the spatial maps of sinusoidal fitting parameters, instead of the raw transmission images, enhances the accuracy of the overlapping assignments. Enhancement in the image stitching accuracy can be attributed to using three sets of data (rather than one) to generate the panorama image.

During the image stitching procedure, two sinusoidal maps are compared at a time. The absolute difference (per pixel) is calculated for possible overlap positions between the images. This calculation is performed for each of the sinusoidal maps:

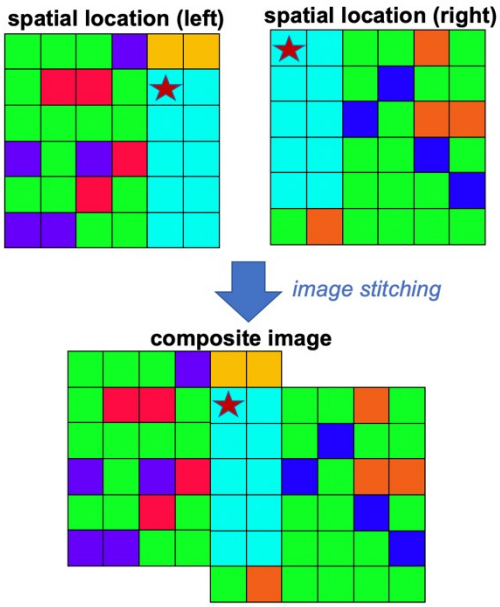

Fig. 7. Schematic representing the image stitching procedure.

Images from two separate spatial locations (left and right) are compared. The red star in both images represents a single feature. Optimal overlap of the images is achieved where this feature is completely overlapped between the two images, as shown in the composite image. Continuing this process for several spatial locations produces a composite image representative of the entire film.

amplitude, phase shift, and vertical offset. Ideal image overlap is illustrated schematically in Fig. 7.

The overall minimum absolute difference is computed from overlapping the three sinusoidal maps. An image overlap position which produces the lowest absolute difference is considered optimal. An ideal overlap position indicates that features of the two images have likely been matched. Once optimal overlap is achieved, the images are blended together using a gradient weighting system to smooth the transition from one image to another.

Assigning mesoscopic domains: Coloring with a quasi-random paint bucket.

Once stitched images have been attained, a systematic method of assigning pixels to discrete domains is necessary to quantify the spatial heterogeneity of the film. By eye, it is straightforward to identify mesoscopic domains within a microscope image. However, picking out each domain manually would be a daunting task, considering that thousands of domains can be present in a single film! Therefore, it is essential to automate the domain assignment process by comparing quantitative measurements indicative of film morphology.

In an image, there are several properties which can distinguish one shape from another. These include brightness, texture, and color[30]. When these properties are quantized and considered synchronously by a computer, pixels within an image can be assigned to distinct objects—which, in this work, we define as mesoscopic domains. There exist numerous, well-established computational techniques for assigning pixels to discrete object as determined by their brightness, texture, and color.

What is a flood fill algorithm?

One such assignment technique is a **flood fill** algorithm[31]. These algorithms are widely implemented in contemporary image processing software. An example of this algorithm can be found in the Microsoft Paint ‘paint bucket’ tool. By utilizing a flood fill algorithm, the interior of a closed shape can be colored radially by clicking on a single pixel in the image.

The premise of a flood fill routine is straightforward. A starting (seed) pixel is first selected by the user. During initialization of the flood fill algorithm, the seed is assigned a particular numerical value. For images, this value is usually descriptive of

color, like RGB. The initial state of the seed (i.e. its numerical value) is stored. As the flood fill algorithm commences, a comparison between the seed and its nearest neighbors is performed. The value of the seed is compared to the value of its nearest neighbors. This comparison elicits a binary response: the seed either does or does not match the neighboring pixel. A binary comparison can occur because every color has a unique RGB value.

The results of the seed-neighbor comparison determine the progression of the flood fill algorithm. If neighboring pixels match the seed, their current numerical value is stored, and they are assigned to the same value as the seed. These matching neighbors are assigned as the next seed pixels. If neighboring pixels do not match the seed, they are ignored and are not assigned to the same numerical value. The flood fill algorithm ends when the seed pixel is surrounded by neighboring pixels that do not meet the match criterion.

What makes our flood fill algorithm distinct?

Conventional flood fill techniques are ideal for discerning shape boundaries where the data are discrete[32]. The flood fill strategy presented in this work diverges from other techniques through its handling of continuous data. The distinction between data types is critical in how pixels are assigned to different domains. In discrete data, a match is rejected if the seed and neighbor do not have identical numerical values. Rather than defining a match as identical, we consider a match for continuous data to be defined by a range of acceptable values. The flood fill algorithm presented in this research employs the phase values (from the sinusoidal fitting routine) as the continuous data for assigning domains.

A quasi-random approach: Guiding the seeds of the flood fill algorithm.

Another necessary consideration in the development of a flood fill routine is the reproducibility of results. Reproducibility is largely determined by the seed pixel. In mainstream flood fill algorithms (like the ‘paint bucket’ tool from Microsoft Paint), input from the user sets the starting pixel. However, a user-defined seed becomes unrealistic when there are thousands of domains to consider within a single image. Automation of the initial seed selection is an ideal strategy to mitigate irreproducibility in the case of domain assignments.

To automate seed selection, the flood fill algorithm presented here considers the standard deviation of phase shift assignments across the surface of the film. The number of neighboring pixels considered in the local standard deviation calculation is set by the user. This calculation builds a spatial map of local deviation in the phase shift assignment. The pixel with the absolute lowest standard deviation in the phase shift parameter is assigned as the first seed. All subsequent seeds are assigned by ascending order of standard deviation values. If a seed has already been assigned to a domain, it is removed from this list of potential seed pixels.

Additionally, boundaries between two domains tend to exhibit more deviation in the phase shift parameter. This trend occurs because pixels in a single domain should possess phase shift assignments distinct to that domain. It follows, then, that the boundary between two domains will contain phase shift assignments characteristic to both domains. If a local standard deviation is computed with pixel contributions from two different domains, the resulting value will likely be much higher than that for a

single domain. As a result, the standard deviation in the phase shift assignments can be used as a guide for which pixels to exclude from consideration as seeds.

Furthermore, the standard deviation map is employed throughout the flood fill routine, during domain assignments. Upon initialization of the routine, the user defines a set threshold to the acceptable range of phase shift values. A threshold of acceptable standard deviations in the phase shift is set manually as well. If a pixel in the spatial map of phase shift standard deviation exceeds the maximal, user-defined threshold, then it is not considered in domain assignments. Unassigned pixels are treated separately from assigned pixels during the quantification of spatial heterogeneity.

Extracting characterization parameters: Defining the sizes, shapes, and orientations of mesoscopic domains.

The flood fill routine outputs a spatial map of unique domains within the film. Once distinct domains have been identified, it is necessary to extract meaningful characteristics out of these domain maps. In this work, three different physical metrics are considered in the quantification of spatial heterogeneity. These domain metrics include area, aspect ratio (***AR***), and intradomain spatial gradation in the phase shift $\left(\frac{d\varphi}{dA}\right)$.

Measuring domain area.

One natural characteristic that arises from the domain data is **area**. Area is defined as the total number of pixels contained within a domain (including edges), converted to a physically significant unit like square millimeters. Domain area is

considered in our analysis of domain metrics because it can be related to the total area of film surface coverage. In other words, we want to probe whether or not there is a correlation between different environmental perturbations and the area of the domains which grow on the film.

Defining a coordinate system for each aggregate domain.

Unlike domain area, $\boldsymbol{AR}$ and $\frac{d\varphi}{dA}$ depend on the orientation of the domain in space. However, the directionality of each aggregate domain is oriented a different way upon the film surface. Therefore, a universal coordinate system cannot be used to describe domain directionality. One reasonable solution is to describe direction-dependent metrics by a **basis set** that is unique to each domain.

A basis set describes the simplest collection of directional components that constitute a physical space. In three dimensions, common basis sets are defined by different **coordinate systems**, the most familiar of which is the Cartesian coordinate system. However, data in this work only examine a two-dimensional space, along the film surface. The depth of a film is not considered. This observation implies that the simplest basis set for each domain will consist of two distinct, orthogonal vectors.

When defining a basis set for different domains, it is necessary to use a mathematical approach that will be reproducible regardless of the domain geometry. One way this condition can be met is by considering the spread of pixels belonging to a single domain. The spread of pixels in the *x*- and *y*-directions is represented as a covariance matrix (see Fig. 8). A covariance matrix describes the spread of pixels that is independent in each direction, as well as the cross-correlated spread.

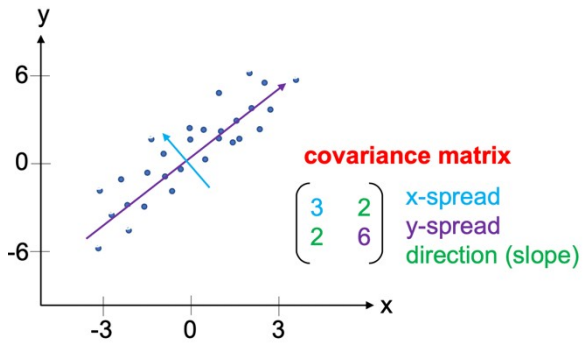

Fig. 8. A schematic representation of assigning a coordinate system using eigenvectors.

An arbitrary set of data is shown with its covariance matrix. The covariance matrix describes the spread of the data in the x- and y-directions, in addition to the covariant spread (i.e. the spread along the diagonal). The arrows overlain on the data represent the coordinate system assigned by using the covariance matrix to solve the characteristic equation (Eq. 2).

The correlation matrix can determine the rotation of the domain from standard coordinates. This determination can be performed by solving the **characteristic equation** of the matrix, which is given by,

$$\det(\mathbf{A} - \lambda\mathbf{I}) = 0, \tag{2}$$

where det is the determinant, **A** is the correlation matrix, λ describes the **eigenvalues** of the system, and **I** is the identity matrix. Further, we can find the direction to which each eigenvalue is associated, called an **eigenvector**, by the equation,

$$\mathbf{A}\vec{x} = \lambda\vec{x}, \tag{3}$$

where $\vec{x}$ is the eigenvector from which we can describe the entire space of the domain.

Using the aspect ratio to describe domain symmetry.

Once an adequate pair of eigenvectors and eigenvalues has been determined for a domain, its **aspect ratio (*AR*)** can also be computed. ***AR*** can be defined as the ratio between the major and minor axes of a shape. In short, ***AR*** considers domain

proportionalities. An ***AR*** value of 1 signifies that the length and width of a domain are very similar. However, ***AR*** >>1 indicates that the domain is very long and thin. If the domain geometry is approximated as an ellipse, the calculated eigenvalues can be used to determine the ***AR*** value of the domain. There exists an eigenvector equation which describes the orientation and size of the ellipse. In this equation, the length of an axis along one eigenvector is set by the square root of the corresponding eigenvalue. Computing the ratio between the "major" and "minor" eigenvalues yields an appropriate measure of the domain ***AR***.

Quantifying intradomain phase shift gradation.

Once a coordinate system has been defined for each domain, an assessment can be made of the magnitude and directionality of phase shift variation within a single domain. We are defining this variation as the **intradomain phase shift gradation** $\left(\frac{d\varphi}{dA}\right)$. There is bound to be some natural gradation in the phase over the spatial coordinates of the domain. This result is due to the fact that the absolute difference in phase shift assignments can vary a finite amount and that pixels are assigned to a domain based upon matching with a neighbor (rather than a statistical average of previously assigned phase shift values).

A value of $\frac{d\varphi}{dA}$ can be determined by computing an averaged two-dimensional gradient of the phase shift values within a single domain. The averaged two-dimensional gradient works by considering the difference between a seed pixel and its nearest neighbors. Gradients maintain their directional components. A local average at a

particular seed pixel is evaluated by taking the statistical mean of gradients from a fixed subsection of pixels within the domain map. Taking a local average gradient helps to smooth over any features (like grain boundaries) which could cause very dramatic changes in the pixel-by-pixel gradient.

Overarching objective: Quantifying the relationship between macroscopic perturbations and the spatial heterogeneity of TIPS-Pn films.

By combining the techniques presented here, we report a homebuilt, polarization-dependent brightfield microscope and computational image analysis method for quantitatively measuring the spatial heterogeneity existent within films of TIPS-Pn. In this work, we demonstrate the functionality of this program by examining a single TIPS-Pn film. Further, several TIPS-Pn films, deposited at different temperatures and with varied solution concentrations, are investigated using the image analysis method. Quantifying the mesoscopic spatial heterogeneity of each film enables insight into how macroscopic perturbations to the deposition environment affect the formation of domains during solution-deposition. Understanding this relationship allows better control over film formation and can contribute toward improving the reproducibility of existing solution-deposition techniques.

Materials and methods: A hybrid experimental-computational technique.

Preparing TIPS-Pn samples: Small scale solution deposition.

Glass substrates (38 mm x 25 mm x 1 mm; VWR 16004-422) were prepared by cleaning the surface with methanol. A 0.400 mL aliquot of a 10 mM trichloro(phenethyl)silane (PETS) in toluene solution was spin-cast onto each substrate to form a wetting layer. The PETS wetting layers were applied under ambient conditions. Solutions of TIPS-Pn in toluene were prepared at concentrations of 1.00, 0.67, and 0.33 mg mL^{-1}. These concentrations were selected because they provide a range of final film thicknesses on the same order of magnitude. During deposition, a 0.300 mL aliquot of the desired TIPS-Pn solution was drop-cast onto the substrate surface using a single channel mechanical pipettor (VWR 89079-974). A Petri dish was used to cover the samples immediately after dropping the TIPS-Pn solution.

To control for environmental perturbations, all films were produced in a homebuilt deposition chamber (see Fig. 9). The deposition chamber isolates the film during deposition from the surrounding room environment. Inside the deposition chamber is a metal sample stage connected to a recirculating bath (VWR AD7LL R-20). The sample stage maintains a constant substrate surface temperature for the duration of the deposition. Film formation was examined at five different deposition temperatures: 30, 40, 50, 60, and 70 °C. These temperatures were selected because they provide a range of film formation times that is on the order of minutes. Film formation on a

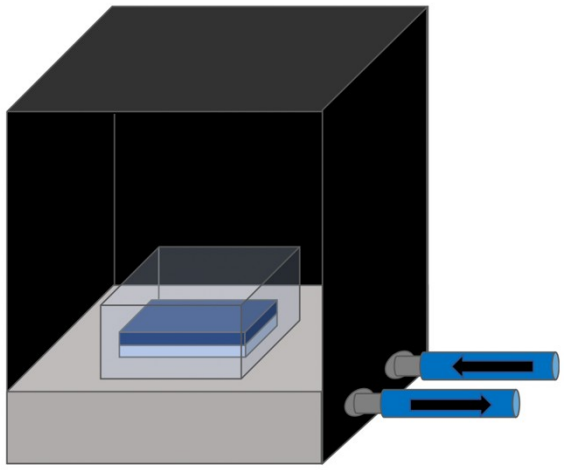

Fig. 9. Homebuilt deposition chamber for drop-casting TIPS-Pn films.

The deposition chamber is an acrylic box that is sealed from the surrounding environment. The sample (blue) rests on an aluminum sample stage (grey). The stage is connected to a recirculating bath (inlet/outlet represented by blue arrows) to control the deposition temperature. A Petri dish (transparent) is placed over the sample immediately after dropping the solution.

timescale of minutes enables an examination of how the rate of solvent evaporation impacts domain formation.

Polarization-dependent brightfield microscopy: imaging the sample.

During the imaging process, a film is secured to the sample stage (Thorlabs XYFM1). A broadband tungsten lamp illuminated the sample. The focal lengths of the objective lens and tube lens are 150 mm. Since these lenses are equal in focal length, there was no magnification to the microscope, as determined by Eq. 1. The detector used in this apparatus is a monochrome camera (Thorlabs DCC1545M). The sensor array of the camera contains 1280 x 1024 pixels. Each pixel in the camera has dimension 5.2 μm x 5.2 μm. Therefore, the camera is capable of imaging a single spatial

location on the film surface with dimensions 6.7 mm x 5.3 mm. Fig. 10 illustrates the optomechanical elements and optical path of a simple brightfield microscope.

Before data acquisition, a series of polarization-dependent background images are collected. Background images measure the transmission of a blank substrate over eighteen polarization angles (0° to 180°), in 10° steps. A linear polarizer is secured to a motorized rotation stage. When collecting sample measurements, only one spatial location on the film is imaged at a time. At maximal transmission, film optical density ranges from ~0.1 to ~0.3. A series of spatial locations is collected over

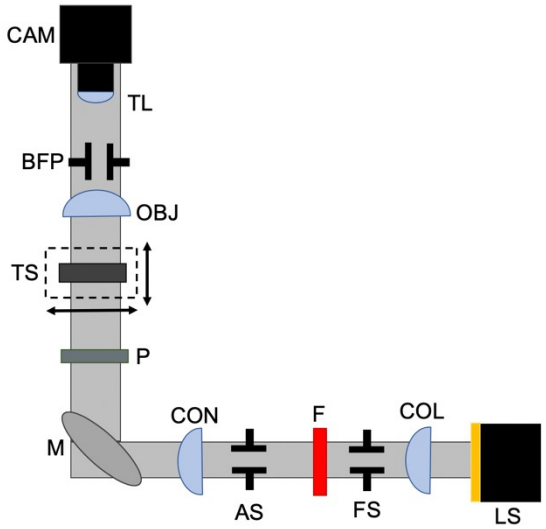

Fig. 10. Experimental setup of the polarization-dependent brightfield microscope.

LS, light source; COL, collector; FS, field stop; F, spectral filter; AS, aperture stop; CON, condenser lens; M, aluminum mirror; P, polarizer; TS, sample plan on a translation stage; OBJ, objective lens; BFP, back focal plane iris; TL, tube lens; CAM, camera. The light source emits light into the optical path. The collector sends this light to the condenser. The condenser reflects vertically off of the aluminum mirror, propagates through the polarizer, and converges at the sample plane. Light transmitted by the sample is directed into the objective lens. The objective lens focuses the light onto the camera detector for image acquisition.

the entire film surface such that they can be constructed into a larger comprehensive map of the sample. At every spatial location, eighteen different polarization images are collected. Pictures of the sample transmission are taken over a range of angle positions on the rotation stage from 0^o to 180^o, in 10^o steps.

Image processing methods.

A sinusoidal fitting routine was built in Python. A best fit curve to the polarization-dependent absorption at each pixel was determined through a least-squares regression routine. Uncertainty in each sinusoidal fit is determined by its indeterminate error. The fit equation is given by Eq. 4,

$$f(x) = A\cos(2\pi x + \varphi) + C \tag{4}$$

where A is the amplitude, φ is the phase shift, and C is the vertical offset.

Twenty spatial locations were used to develop a panoramic image of each film. These images yielded a total area of ~600 mm^2 . For the domain identification algorithm, approximately 200,000 seeds were selected. The eight nearest neighbors were considered for every seed. Standard deviation thresholds considered for separation of domains were 2.5°, 3.5°, 4.5°, and 5.5°. Flood fill thresholds considered for separation of domains were 3.0°, 4.0°, 5.0°, and 6.0°. Approximately 200-1000 domains were identified for each film.

Results and discussion: A complete demonstration of the image processing procedure.

In this work, we use polarization images collected over the entirety of a single film to show how the homebuilt image analysis technique is applied. A film produced at 60 °C with a solution concentration of 1.00 mg mL^{-1} demonstrates the image processing method.

Converting raw transmission images into absorption measurements.

Fig. 11 shows a series of absorption images collected at a single spatial location on the sample. The absorption value at each pixel within the image is computed by normalizing raw transmission values collected by the camera. Absorption values are computed by

$$A = -\log_{10}\left(\frac{T}{T_0}\right) \tag{5}$$

where A is the absorption, T is the measured transmission, and T_0 is the background transmission recorded at a single polarization angle (with a blank slide in place). Absorption measurements are reported as optical density in this work.

The spatial location highlighted in Fig. 11 is located toward the outer periphery of the film, where more discrete domains are observed. In Fig. 11, each image shows the absorption at a particular polarization angle, which is listed above the image. Comparing the eighteen different absorption images, it is clear that particular crystalline structures absorb more or less with respect to the polarization of the incoming light.

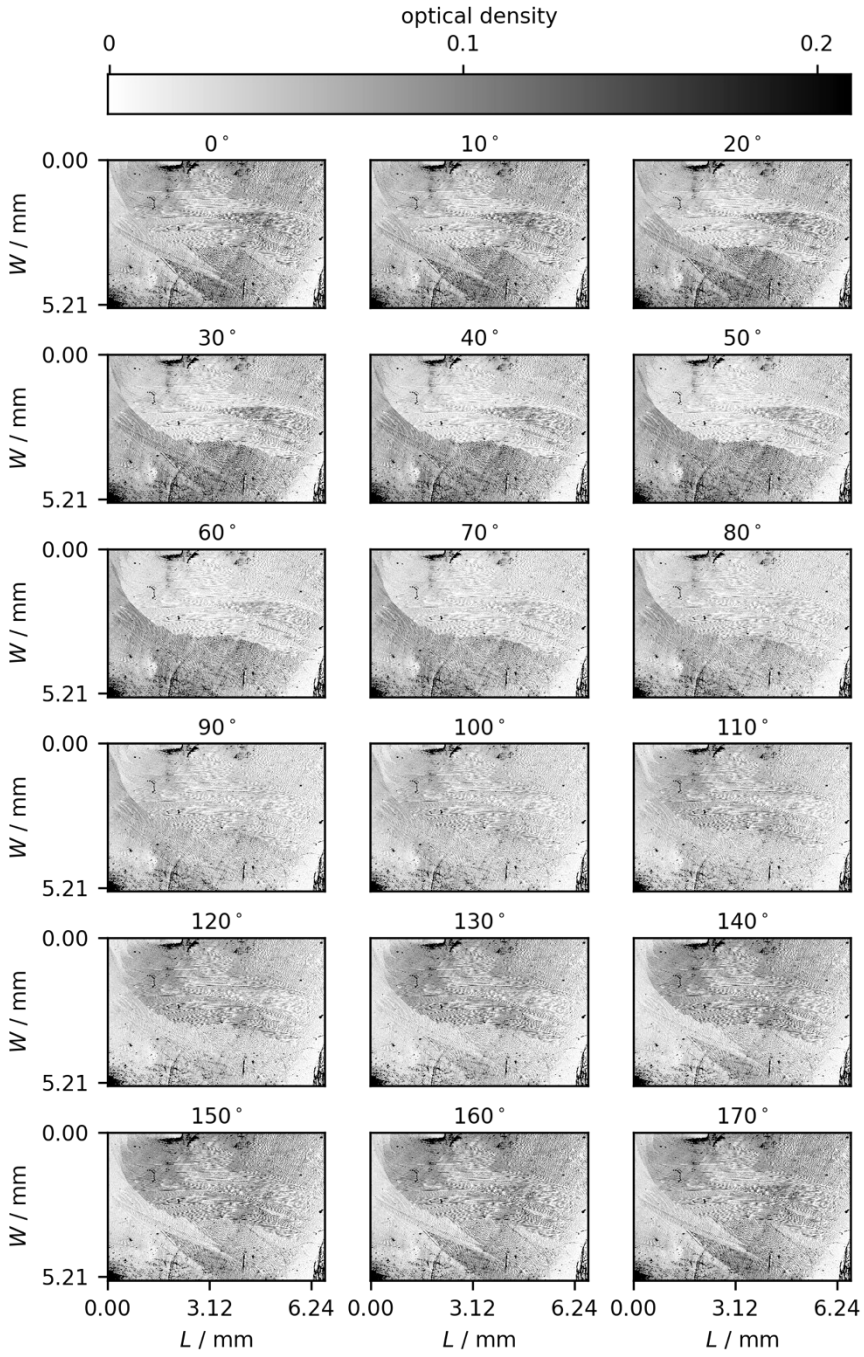

Fig. 11. A series of absorption images collected at a single spatial location.

Between each image, the polarizer is rotated ten degrees. The relative polarization angle of the polarizer is listed above the image of the film. Dimensions of the film (*L*, length; *W*, width) are converted from pixels to millimeters by a factor of 5.2 mm/pixel. Crystalline structures within the sample absorb more or less light depending on their physical orientation relative to the polarization of the incoming light.

It is also in Fig. 11 that we can observe the expected oscillatory absorption behavior as a function of polarization angle.

Fitting polarization-dependent absorption measurements to sinusoidal waveforms.

Since the absorption of every pixel in Fig. 11 is periodic as a function of polarization angle, it can be fit to a sinusoidal curve. Fig. 12 demonstrates this sinusoidal curvature. The five colored stars in Fig. 12(a) show the five select pixels used for demonstration. The colored markers in Fig. 12(b) exhibit the absorption at the single pixel as a function of polarization angle, while dashed lines demonstrate the sinusoidal fit to the measured data. Marker and trace colors shown in Fig. 12(b) correlate to the pixels highlighted by the colored stars in Fig. 12(a).

Polarization-dependent absorption measurements illustrated in Fig. 12(b) demonstrate the relative orientations between crystalline structures, which can be

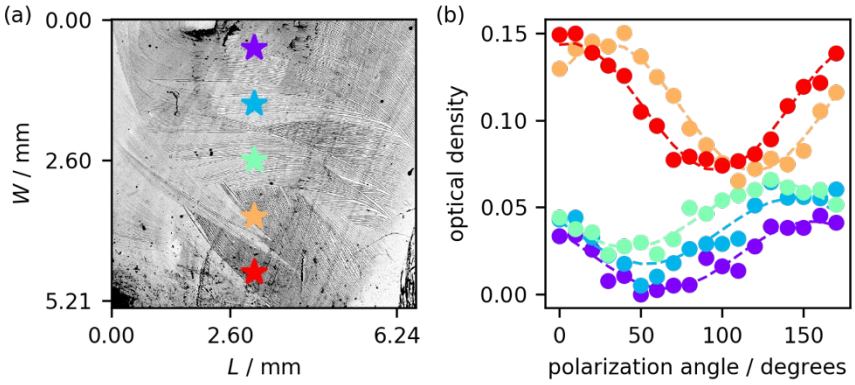

Fig. 12. Sinusoidal absorption (at individual pixels) as a function of polarization angle. Five pixels from the absorption spatial map at a polarization angle of 0° (see Fig. 11) are highlighted, as indicated by the colored stars in (a). The corresponding absorption measurements as a function of polarization angle are shown as colored dots in (b). Dashed lines in (b) show the sinusoidal fit of the data. Colored traces in (b) correspond to the same colored star in (a).

inferred by examining the positions of the maximal peaks of the fits (dashed lines). Observe that the minimum of the orange and red traces shown in Fig. 12(b) occur where the purple, blue, and green traces approach their maximum absorption values. This behavior suggests that the crystalline structures marked by the orange and red stars are rotated in the spatial plane approximately ninety degrees relative to the structures marked by the purple, blue, and green stars.

A qualitative examination of the crystalline structures shown in Fig. 12(a) can be used to confirm the differences in their relative orientations, shown in Fig. 12(b). As displayed in Fig. 12(a), structures marked by the orange and red stars exist within regions of the sample with a high optical density (~0.10-0.15). Meanwhile, structures marked by the purple, blue, and green exist within regions of the sample with a low optical density (~ 0.05-0.10). Crystalline structures that exhibit different optical densities at the same polarization angle could be described by different sinusoidal absorption curves. Alternatively, this observation could suggest that there is a difference in film thickness between these two regions. The sinusoidal transmission behavior for different spatial locations on a single film is illustrated in Fig. 12(b).

While Fig. 12 shows the absorption as a function of polarization angle for individual pixels, this sinusoidal behavior can be fit for all pixels within the image. Fig. 13 illustrates the sinusoidal fitting parameters (amplitude, phase shift, and vertical offset) as a function of spatial coordinates. In other words, Fig. 13 shows the sinusoidal fitting parameters that correspond to polarization-dependent absorption values assigned to each pixel. We can clearly observe in Fig. 13(b) that pixels of uniform phase shift tend to reveal boundaries between the crystalline structures observed by eye.

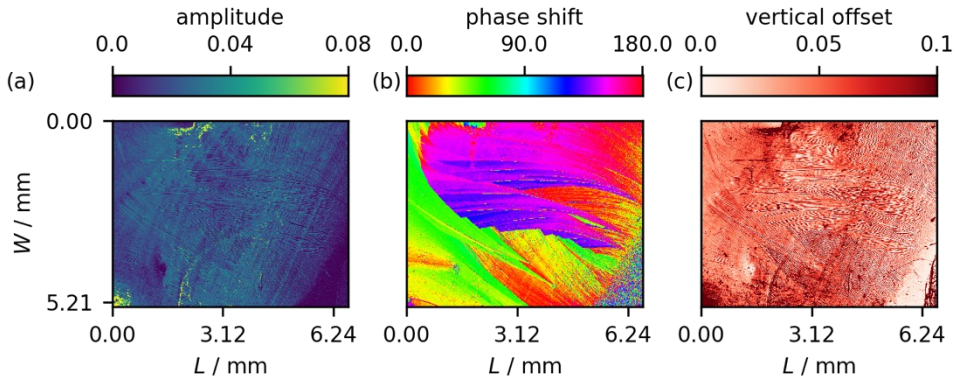

Fig. 13. Spatial maps of the (a) amplitude, (b) phase shift, and (c) vertical offset of sinusoidal fitting parameters at a single location on the film.

Each map above enables a spatial comparison of the fitting parameters generated for each individual pixel. These parameters are extracted from the sinusoidal absorption measurements demonstrated in Fig. 12(b).

Comparing Fig. 13(b) to Fig. 12(a), the spatial map of phase shifts exposes the crystalline structures which can be considered as belonging to the same domain.

Notice also in Fig. 13(b) that the phase shift values are cyclic. This property arises from the oscillatory nature of sinusoidal functions. As a result, the color values representing the phase shift scale are also cyclic. We should not expect strong divisions between phase values of 180^{o} and 0^{o} because these are, in essence, the same phase angle assignment.

Boundaries between crystalline structures are not as obvious in the spatial maps of amplitude and vertical offset, as can be observed in Fig. 13(a) and Fig. 13(c), respectively. This observation arises from the physical interpretation of the sinusoidal fitting parameters. Since the amplitude measures relative film thickness across the surface of a sample, ideally it should not vary dramatically in a sample with uniform surface coverage. A rather narrow range of amplitude fits (~0.02-0.04) is observed across the surface of this spatial location on the sample. Similar to the amplitude, the

vertical offset should not vary substantially because it represents the local average thickness at a particular pixel location. As expected, a small range of vertical offset values (~0.02-0.07) is exhibited in Fig. 13(c).

Building panorama images.

Even though large structural features cannot be observed in the spatial maps of amplitude and vertical offset fits, these data can still be used, in combination with the spatial map of phase shift assignments, to build a comprehensive view of the sample (see Fig. 14). All three spatial maps of fitting parameters are employed to stitch together several spatial locations along same film. The resulting output is shown in Fig. 14, which illustrates a cohesive map of phase angle assignments across the entire surface of

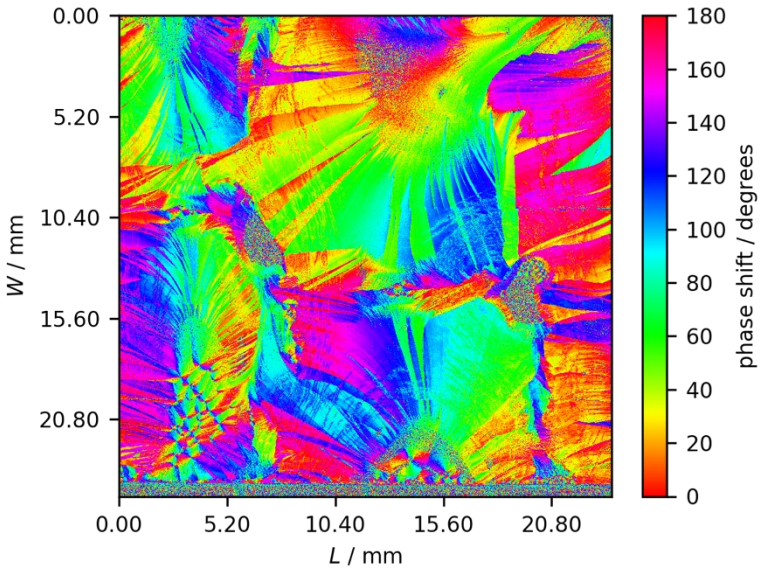

Fig. 14. Complete spatial map of phase shift assignments on a single film.

This map enables a qualitative assessment of the spatial morphology of the film. Dramatic differences in the phase shift values between neighboring pixel groups can visually confirm the presence of what we are describing as a discrete domain.

the sample. Fig. 14 enables an assessment of the discrete crystalline domains which comprise the film.

Domains can be qualitatively determined by examining the stark boundary lines illuminated by the phase shift assignments. We can qualitatively observe in Fig. 14 that there are a variety of different domains occupying the surface of the film. These domains range from long, narrow geometries to elongated trapezoidal structures. In this particular film, most observed domains appear to be 2-5 mm in length.

Identifying mesoscopic domains within a film.

In addition to a qualitative view, the spatial phase shift map can also be employed in a quantitative evaluation of domains contained within a film. A quantitative assessment of domains is performed by utilizing the complete phase shift map in the domain identification routine. One essential component used in this routine is a spatial map describing the local standard deviation of phase shift values, represented as $\boldsymbol{\sigma_{ph}}$. These maps define the boundaries between discrete domains. The threshold of permissible deviation in the phase shift, denoted as $\boldsymbol{\beta_{std}}$, controls the strictness of domain boundaries. Fig. 15 illustrates how boundary strictness varies with $\boldsymbol{\beta_{std}}$.

As observed in Fig. 15, adjusting the value of $\boldsymbol{\beta_{std}}$ changes the boundary lines between domains. However, domain assignments are not obvious from these spatial maps of $\boldsymbol{\sigma_{ph}}$ alone. Rather, standard deviation maps must be paired with the homebuilt domain identification routine to systematically assign discrete domains within a film. Threshold parameters—which include both $\boldsymbol{\beta_{std}}$ and the flood fill threshold, $\boldsymbol{\beta_{ff}}$—are selected for use in the domain identification routine from a calibration matrix, shown in

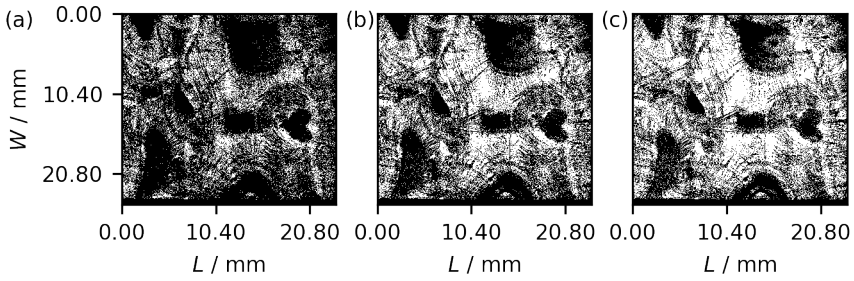

Fig. 15. Spatial map of σ_{ph} as a function of β_{std}.

Spatially mapping the deviation in the phase shift guides boundary decisions within the domain identification routine. These maps are generated using β_{std} = 2.5° (a), 3.5° (b), and 4.5° (c). Colors representing the data are binary. A value of 1 (black) indicates that $\sigma_{ph} > \beta_{std}$, meaning that a boundary exists at this location. Conversely, a value of 0 (white) translates to $\sigma_{ph} \leq \beta_{std}$, indicating that is unlikely for a boundary exists at this location.

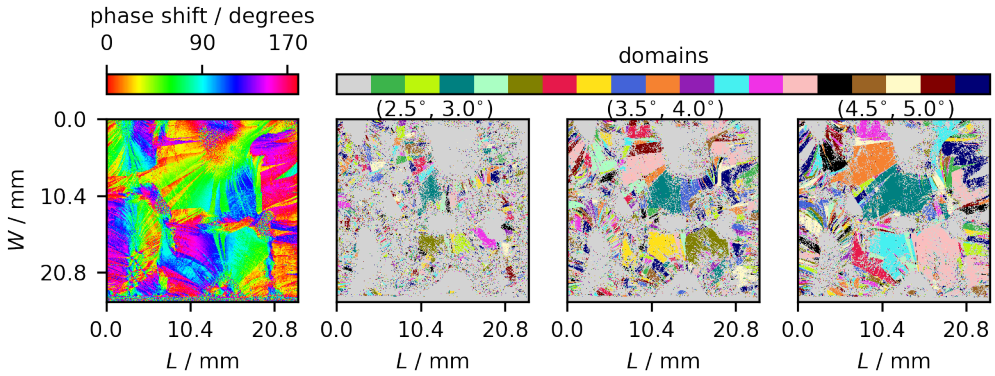

Fig. 16. Calibration matrix for determination of ideal domain identification parameters.

The grid of images demonstrates how the spatial domain map, produced with the domain identification routine, changes as a function of both β_{std} and β_{ff} values. Gray areas represent spatially heterogeneous regions of the film that could not be assigned with the program. The color scale describes that domains are distinct. The (4.5°, 5.0°) domain map exhibits the most ideal identification of domains. As a result, the threshold combination of (4.5°, 5.0°) is used in further characterization procedures.

Fig. 16. The calibration matrix enables a visual evaluation of which $\boldsymbol{\beta_{std}}$ and $\boldsymbol{\beta_{ff}}$ values are ideal for building a domain map. Threshold parameters are considered "ideal" when the domain map produced aligns with our qualitative assessment of domain assignments.

Fig. 16 demonstrates that the combination of identification parameters considered optimal for this film are $\boldsymbol{\beta_{std}}$ = 4.5°and $\boldsymbol{\beta_{ff}}$ = 5.0°. These values indicate that $\boldsymbol{\sigma_{ph}}$ > 4.5° will result in a domain boundary, and that local (pixel-to-pixel) similitude in phase shift assignments will be less than 5.0°. Further analysis of the domains within the film will be performed on the domain map shown in Fig. 16, with threshold values of $\boldsymbol{\beta_{std}}$ = 4.5° and $\boldsymbol{\beta_{ff}}$ = 5.0°.

Calculating domain metrics to describe spatial heterogeneity.

Once ideal values of $\boldsymbol{\beta_{std}}$ and $\boldsymbol{\beta_{ff}}$ have been determined, physical characterization metrics—size and ***AR***—can be extracted from the resulting domain map. Values of $\frac{d\varphi}{dA}$ were not considered in this work due to a computational runtime error. These metrics are obtained by using the domain characterization routine. Each domain within the domain map is considered individually when determining its physical characterization metrics. Fig. 17 shows the definition of a single domain within the spatial map of phase shift values.

Once a domain has been isolated, as illustrated in Fig. 17, its physical characterization metrics can be determined. Fig. 18 visually demonstrates these metrics for the single domain highlighted in Fig. 17.

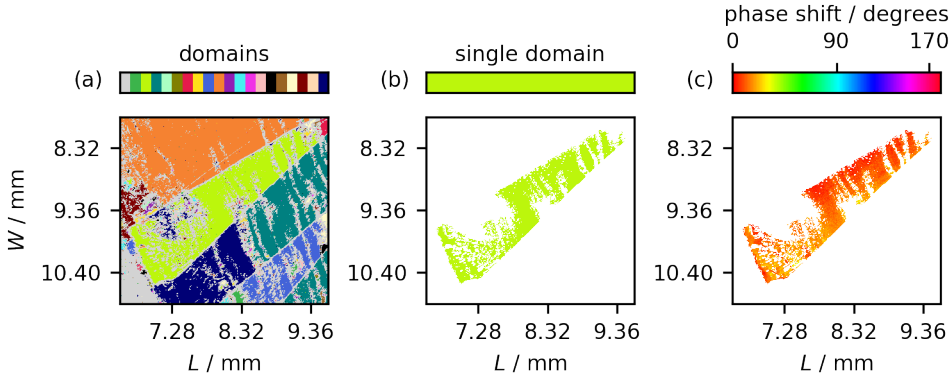

Fig. 17. Using the domain map to define a single domain within the film.

The spatial map of domains shown in (a) is a small subset of data, cropped from (4.5°, 5°) domain map shown in Fig. 16. This region was selected to highlight the single domain, shown in (b). The image illustrated in (b) demonstrates how single domains are isolated from the complete domain map. Isolating domains enables computation of physical characterization metrics on a domain-by-domain basis. In (c) the spatial map of phase shift values is shown exclusively for the domain highlighted in (b).

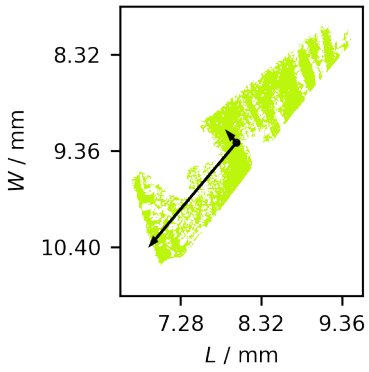

Fig. 18. Visual representation of domain characterization metrics.

An isolated domain is shown, along with its corresponding eigenvectors. This image is reproduced from Fig. 17(b), with the eigenvectors overlaid. The magnitudes of the eigenvalues are scaled by a factor of 150. The ***AR*** is determined to be 4.3.

Each domain within the spatial phase shift map is isolated (as demonstrated in Fig. 17) and will contain a unique set of characterization metrics (as shown in Fig. 18). A distribution of domain sizes and ***AR*** values can be determined by computing these metrics for every domain in the film. Fig. 19 shows the distribution of domain areas, aspect ratios, and spatial phase shift gradation evaluated for a single film.

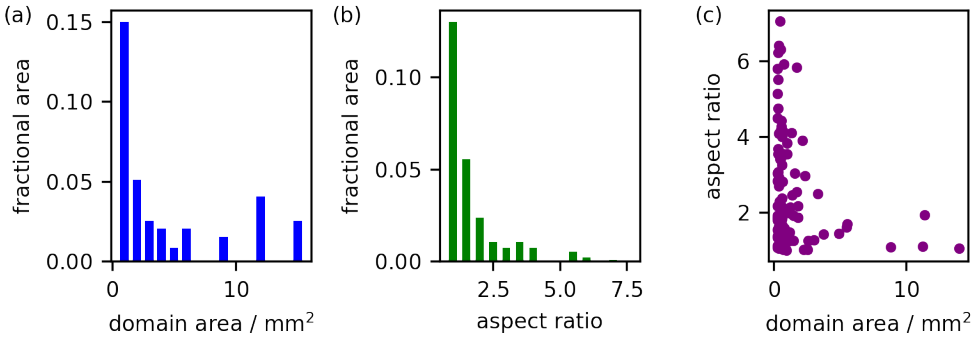

Fig. 19. Distribution of areas, ***AR***, and ***AR*** vs. area for all domains within a single film. (a) Distribution of domain sizes; (b) distribution of domain ***AR*** values; and (c) correlation plot of ***AR*** as a function of domain area.

Fig. 19 demonstrates that the majority of the film surface (~25%) is composed of domains with area measurements < 5 mm^2. Similarly, values of ***AR*** < 2.5 appear to be the most prominent contributors to the film composition. By comparing ***AR*** to domain size, it is clear that there is not a definitive trend between ***AR*** and domain area. This conclusion can be drawn from the fact that domains with areas < 5 mm^2 appear to sample all of the ***AR*** values. Additionally, there appears to be a large population of domains that have ***AR*** values < 2.5, independent of domain size. This result is consistent with the distribution presented in Fig. 19(b).

As we can see from Fig. 19, the image analysis package described in this work provides a quantitative measure of spatial morphology through calculation of domain

characterization metrics. However, in order to draw meaningful connections between the macroscopic deposition and film spatial heterogeneity, it is necessary to apply this technique to several films.

Results and discussion: How do deposition temperature and solution concentration affect spatial heterogeneity?

The technique presented in this work for quantification of film spatial heterogeneity can be applied to several films produced at various deposition conditions. This section compares the spatial heterogeneity for a series of films produced under varied deposition temperatures and solution concentrations. In this analysis, spatial heterogeneity is described by two domain metrics: area and $\boldsymbol{AR}$. Values of $\frac{d\varphi}{dA}$ were not computed for these data because of a computational runtime error. Measuring the spatial heterogeneity as a function of deposition conditions will provide insight into how these environmental perturbations affect the formation of mesoscopic domains.

Using a calibration matrix to determine optimal values of β_{std} and β_{ff}.

Two films were prepared at each combination of deposition temperature and solution concentration. Individual transmission images collected for each film were converted to panoramic spatial maps of sinusoidal fitting parameters, as described in the section, *Results and discussion: A complete demonstration of the image processing procedure***.** A calibration matrix, similar to that presented in Fig. 16, is shown in Fig. 20. The films displayed in Fig. 16 have a concentration of 1.00 mg mL^{-1}. Only one of the two films prepared at each combination of solution concentration and deposition temperature is considered. The domain maps shown in Fig. 16 were produced using the following combinations of $\boldsymbol{\beta_{std}}$ and $\boldsymbol{\beta_{ff}}$, denoted as ($\boldsymbol{\beta_{std}}$, $\boldsymbol{\beta_{ff}}$): (3.5^o, 4.0^o); (4.5^o, 5.0^o); and

(5.5°, 6.0°). For each set of three domain maps, the corresponding map of phase shift fits is also shown.

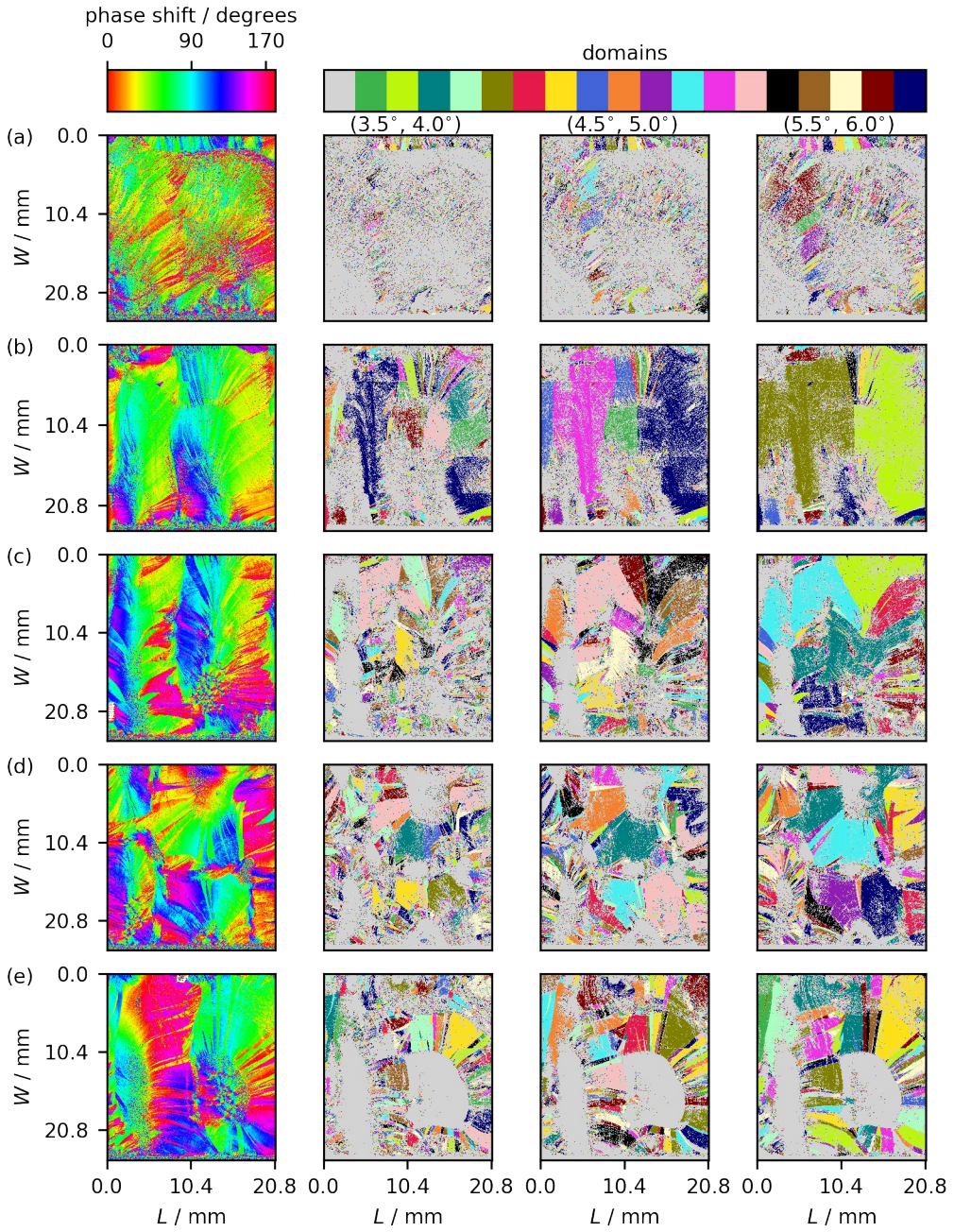

Fig. 20. Calibration matrix for determination of optimal $\boldsymbol{\beta}_{std}$ and $\boldsymbol{\beta}_{ff}$ values.

All films shown were produced with a solution concentration of 1.00 mg mL^{-1}. Only one film is shown for every deposition temperature at this concentration. Rows correspond to deposition temperature: (a) 30 °C, (b), 40 °C, (c) 50 °C, (d) 60 °C, and (e) 70 °C. The first column shows the spatial phase map of each film. Remaining columns indicate the combination of ($\boldsymbol{\beta}_{std}$, $\boldsymbol{\beta}_{ff}$) employed for generation of domain maps in that column.

Several domain maps shown in Fig. 20 exhibit large grey regions. Grey regions signify that the pixels at these spatial locations are unassigned to a particular domain. Failure to assign pixels to a domain occurs due to the extreme spatial heterogeneity observed in those regions of the film. One example of this effect can be observed in the film deposited at 70 °C. For all combinations of $\boldsymbol{\beta}_{std}$ and $\boldsymbol{\beta}_{ff}$ at this temperature, there exists a large, grey region in the lower righthand corner of the film. Comparing these domain maps to their corresponding phase shift map reveals that there are a large quantity of small, radial structures. These radial structures exhibit a diverse collection of phase shifts. A high diversity of phase shift assignments in one spatial region indicates that these pixels do not describe a single domain. Consequently, the domain identification algorithm refrains from assigning these pixels to discrete domains.

There is an inherent tradeoff between domain resolution and the magnification of the brightfield microscope instrument. Resolving unassigned domains within a film would require that images be collected at higher magnifications. At higher magnifications, more pixels in the camera detector are assigned to a particular spatial location on the film, providing more resolution. However, increasing the magnification of the microscope would, inherently, decrease the size of the viewing window. In turn, improvements to domain resolution require additional data acquisition time and computational power for stitching the images together. While higher resolution of domains is ideal for describing microscopic domains (area < 0.5 mm^2), it is not ideal given the current experimental design and objectives presented in this work.

The overarching utility of Fig. 20 is to determine which values of $\boldsymbol{\beta_{std}}$ and $\boldsymbol{\beta_{ff}}$ best represent the mesoscopic domain assignments observed by eye. While some of the differences between domain maps can be subtle, there are a few key features which can reveal the ideal combination of $\boldsymbol{\beta_{std}}$ and $\boldsymbol{\beta_{ff}}$ to use. Examining the domain maps produced at a single temperature as a function of $\boldsymbol{\beta_{std}}$ and $\boldsymbol{\beta_{ff}}$ combination will expose which threshold parameters best reflect the true domain assignments.

Examination of the (5.5°, 6.0°) domain maps show that the domain features seem to merge together more in this parameter combination than in domain maps generated by (3.5°, 4.0°) or (4.5°, 5.0°). Merging of features, in these data, is not an accurate representation of the film morphology. This observation can be validated through the spatial phase maps shown in Fig. 20. The phase shift maps for these films display a large quantity of small pixel groups containing the same phase shift assignment. This observation suggests that several smaller domains, rather than fewer large domains, would be an ideal representation of structural morphology in these films.

The domain maps corresponding to the films deposited at 40 °C and 50 °C, shown in Fig. 20(b-c), can be used to reject the threshold parameter combination of (5.5°, 6.0°). For the 40 °C film, observe that the domain map produced at (5.5°, 6.0°) consists of only two major domains. However, remaining domain maps, (3.5°, 4.0°) and (4.5°, 5.0°), separate these two features into several smaller aggregate domains. Examination of the spatial phase shift map suggests that features on the top right quadrant of the film should be separated into distinct domains. The combination (5.5°, 6.0°) does not reflect this separation of features. An additional example can also be drawn from the 50 °C film. The light blue domain in the (5.5°, 6.0°) map engulfs a

smaller feature which, as suggested by the phase shift map, should be separated into a different discrete domain. Therefore, it is unlikely that (5.5°, 6.0°) is an ideal reflection of domain assignments.

Comparing the domain maps produced for a single film to their corresponding phase shift map can also reveal when a threshold combination is too strict in domain assignments. While a strict threshold combination may accurately separate pixels into distinct domains, the resulting domains assigned may exhibit a smaller area on the film than the spatial phase shift map would suggest. The ideal threshold strictness can be determined by, again, looking to Fig. 20.

The domain maps generated at (3.5°, 4.0°) and (4.5°, 5.0°) for the 50 °C film can be employed in the determination of ideal threshold strictness. Observe the large, light pink feature in the upper left quadrant of both domain maps. While it maintains the same general shape in both domain maps, the area of this feature is reduced substantially in the (3.5°, 4.0°) combination compared to the less strict combination of (4.5°, 5.0°). The phase shift map describing the 50 °C film suggests that this feature should have a larger area, more comparable to that exhibited in the (4.5°, 5.0°) map. A similar observation can be made for the teal feature seen near the center of the (3.5°, 4.0°) and (4.5°, 5.0°) for the 60 °C film. This domain is almost twice as large in the (4.5°, 5.0°) domain map as in the (3.5°, 4.0°) domain map. The phase shift map for the 60 °C film suggests that the feature should constitute an area best represented by the (4.5°, 5.0°) domain map. These results confirm that the ideal threshold combination is $\boldsymbol{\beta}_{std}$ = 4.5° and $\boldsymbol{\beta}_{ff}$ = 5.0° for the films presented in this work.

Choosing domain maps for quantification of spatial heterogeneity.

After determining an ideal combination of threshold parameters, domain maps produced at this combination can be compared to choose the best subset of domain maps for a quantitative analysis of spatial heterogeneity. The (4.5°, 5.0°) domain map for the film produced at 30 °C shows that the majority of the film area is unassigned. In other words, the 30 °C film exhibits a high degree of spatial heterogeneity, thus producing a sparse domain map with large regions of unassigned pixels. Large unassigned regions of the film will not yield meaningful results in the determination of domain metrics. As a result, this film will be omitted from further analysis.

At 40 °C, large sections of the surface are dominated by a single domain as shown by the large bright pink and dark blue domains. While the 40 °C film contains domain assignments, the phase shift map illustrates that some domain assignments at the (4.5°, 5.0°) threshold combination were invalid. This discrepancy can be observed on the righthand edge of the film. The phase shift map suggests that several smaller domains should exist on the righthand edge of the 40 °C film, whereas the domain map presents a single domain in this region. Due to this discrepancy, we should omit this data from the discussion of domains identified by the (4.5°, 5.0°) threshold combination.

Though not shown, resulting domain maps for films produced at concentrations of 0.33 mg mL^{-1} presented mostly unassigned pixels. These data can also be omitted because they will not provide meaningful results in the domain quantification routine. Consequently, further results presented in this work will focus exclusively on films

deposited at temperatures of 50, 60, and 70 °C, as well as from solutions with concentrations of 1.00 mg mL^{-1} and 0.67 mg mL^{-1}.

Quantitative determination of domain metrics.

Domain maps considered for quantitative analysis were generated using a threshold combination of $\boldsymbol{\beta_{std}}$ = 4.5° and $\boldsymbol{\beta_{ff}}$ = 5.0°. Domain metrics describing area and ***AR*** are calculated as described in the section, *Results and discussion: A complete demonstration of the image processing procedure*. Distributions of domain metrics are visualized against fractional area, rather than the number of counts (as in a conventional histogram). We are defining fractional area as the area occupied by a single domain compared to the total area of the two films combined. This visualization strategy reveals how much of the film surface is dominated by a particular domain size or ***AR***.

Examining domain size as a function of deposition temperature and solution concentration.

The effect of deposition temperature and solution concentration on domain size can be quantified by considering the temperature- and concentration-dependent distributions of domain area. Fig. 21 shows the fractional area as a function of domain area. Results in Fig. 21 are shown for two replicate films.

Distributions are compared as a function of deposition temperature and solution concentration. It is evident from Fig. 21 that the overall distribution of domain sizes is approximately the same for all combinations of deposition temperature and solution concentration. In all plots displayed in Fig. 21, there is a sharp peak at domain area

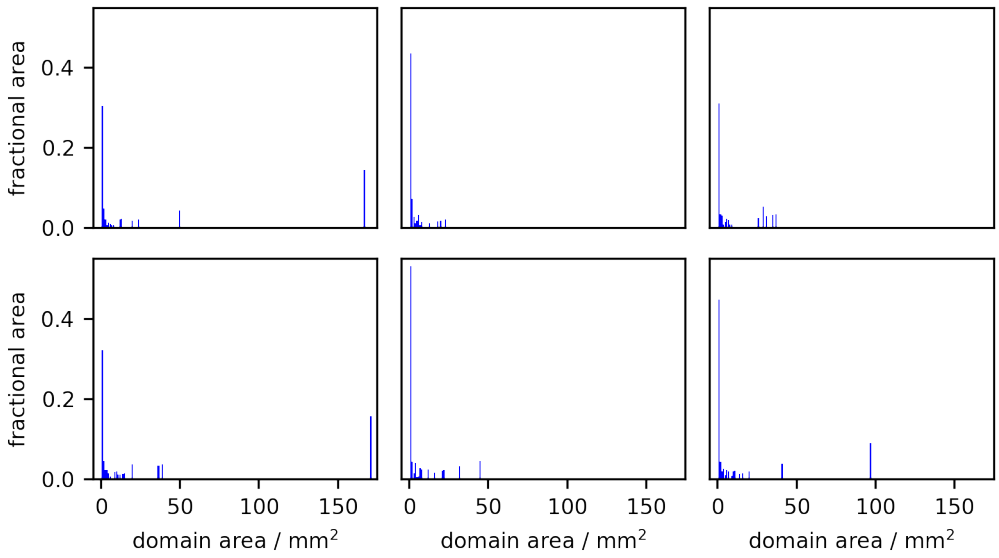

Fig. 21. Fractional area occupied by all measured domains.

Rows correspond to solution concentrations of 0.67 mg mL^{-1} (top) and 1.00 mg mL^{-1} (bottom). Columns correspond to deposition temperatures of 50, 60, and 70 °C (left to right). The histograms are binned in 1.0 mm^2 steps.

values of 0-5 mm^2. These domains constitute a high percentage of the total film, ranging from 30-50% of the total film area.

The only conclusion that can be drawn from Fig. 21 is that a high population of small domains (area < 25 mm^2) exist within each film. However, from this scale of domain areas, it is challenging to observe any meaningful trends in the distribution of small domains as a function of temperature and concentration. Fig. 22 reproduces Fig. 21, limiting the area metric to domains less than 25 mm^2.

Even with a change in scale, the relationship between deposition temperature, solution concentration, and domain size is still not clear from Fig. 22. The distribution of domain area decays exponentially for all deposition temperatures and solution concentrations. The only major difference between plots shown in Fig. 22 is the magnitude of the total film surface occupied by domains of area 0-1 mm^2. For the film

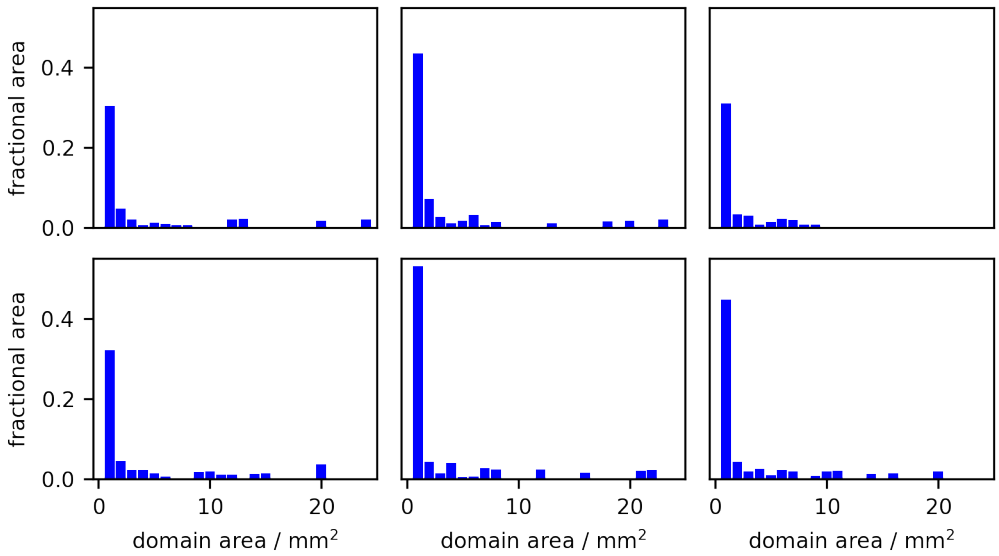

Fig. 22. Fractional area occupied by small domains (area < 25 mm^2).

Rows correspond to solution concentrations of 0.67 mg mL^{-1} (top) and 1.00 mg mL^{-1} (bottom). The columns correspond to deposition temperatures of 50, 60, and 70 °C (left to right). The histograms are binned in 1.0 mm^2 steps.

produced at 60 °C with a concentration of 0.67 mg mL^{-1}, ~41% of domains exhibit area measurements between 0-1 mm^2. For films produced at 60 °C with a concentration of 1.00 mg mL^{-1}, it is ~50%. These values are about 10% higher than those reported for films at 50 and 70 °C at both solution concentrations.

While the raw magnitudes of 60 °C film peaks may be higher than for other deposition temperatures, this trend is likely due to a higher quantity of small domains existing within the film. In other words, the results presented in Fig. 21 and Fig. 22 do not demonstrate a substantial difference between the fractional area and domain size in films produced at 50, 60, and 70 °C with solution concentrations of 0.67 mg mL^{-1} and 1.00 mg mL^{-1}. It is clear from the data that environmental perturbations were not able to control domain size in these films.

Examining aspect ratio as a function of deposition temperature and solution concentration.

A similar examination of ***AR*** can also be conducted. Fig. 23 illustrates the fractional area as a function of domain aspect ratio. Results in Fig. 23 are shown for replicate films produced under the same environment conditions.

Fig. 23 shows that the distribution shapes are approximately the same for all temperature and concentration combinations. There are no clear trends in the data that can be observed from Fig. 23. Akin to the analysis of the domain sizes, the ***AR*** axis of the distributions can be rescaled to consider only domains with small ***AR*** values (***AR*** ≤ 10). Fig. 24 reproduces Fig. 23, rescaling the ***AR*** axis.

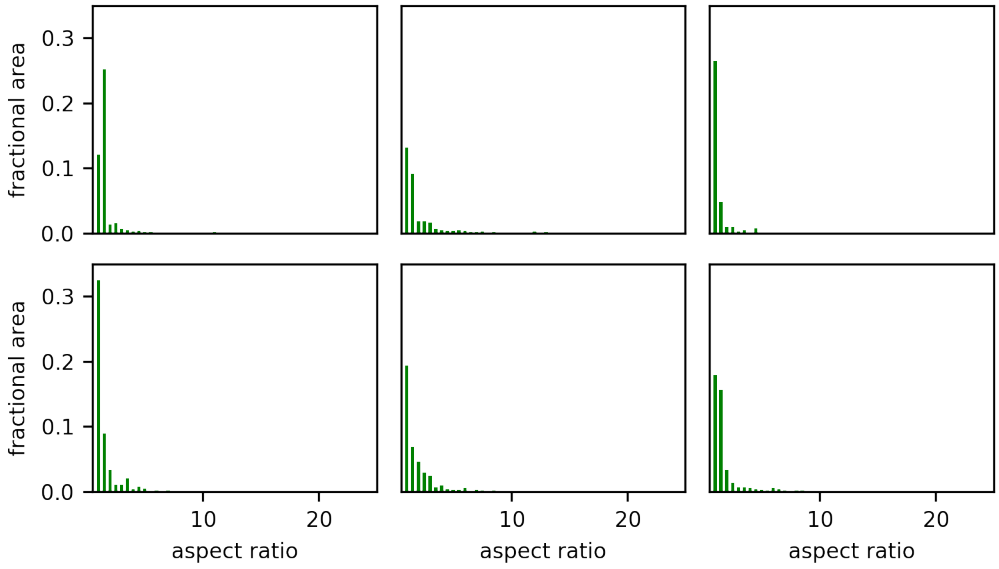

Fig. 23. Fractional area as a function of domain ***AR*** for all domains measured.

Rows correspond to solution concentrations of 0.67 mg mL^{-1} (top) and 1.00 mg mL^{-1} (bottom). Columns correspond to deposition temperatures of 50, 60, and 70 ^{o}C (left to right). The histograms are binned in ***AR*** steps of 0.5.

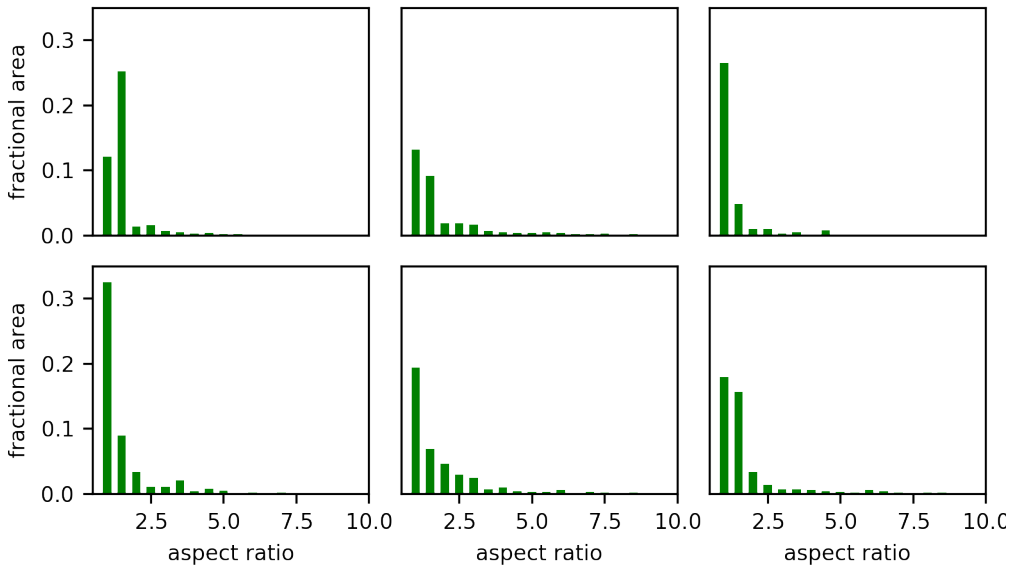

Fig. 24. Fractional area as a function of domain ***AR***, for domains with small ***AR*** values (***AR*** $\leq$ 10).

Rows correspond to solution concentrations of 0.67 mg mL^{-1} (top) and 1.00 mg mL^{-1} (bottom). Columns correspond to deposition temperatures of 50, 60, and 70 °C (left to right). The histograms are binned in ***AR*** steps of 0.5.

The rescaled distributions shown in Fig. 24 can provide insight into how the ***AR*** distributions change with deposition temperature or solution concentration. Consider the ***AR*** distributions at a single temperature. Fig. 24 shows that, for one deposition temperature, the ***AR*** distributions for films produced at a solution concentration of 0.67 mg mL^{-1} may decay more rapidly than for films produced at 1.00 mg mL^{-1}. In other words, domains with ***AR*** values greater than two constitute about 10% of the total film area when the solution concentration is 1.00 mg mL^{-1}, and less than 5% when the solution concentration is 0.67 mg mL^{-1}. However, given that only two films were considered during analysis, there is not enough evidence to definitively claim that a relationship exists between solution concentration and the width of the ***AR*** distribution.

For the most part, Fig. 23 and Fig. 24 demonstrate that the ***AR*** distribution shape is independent of temperature and concentration. As a result, no conclusions can be drawn regarding the effect of deposition temperature and solution concentration on the observed ***AR*** values within a film.

Correlating aspect ratio to domain size as a function of deposition temperature and solution concentration.

One final comparison can be made between domain size and domain ***AR***. Visualizing these data simultaneously as a function of both temperature and concentration can reveal any correlations between the size of a domain and its relative length-to-width ratio. Fig. 25 displays the domain ***AR*** as a function of domain area, for small domains (area ≤ 25 mm^2) and small ***AR*** values (***AR*** ≤ 10). Only small domains and small ***AR*** values were considered to highlight any trends in peak broadening that result because of deposition temperature or solution concentration.

Fig. 25 illustrates that a sharp peak exists in the ***AR*** data as a function of domain size. This peak is located between area values of 0-1 mm^2 and occurs for all combinations of deposition temperature and solution concentration. The distributions shown in Fig. 25 are, for the most part, very similar. However, there exist a few minor differences between these distributions. It can be observed that the distribution for films produced at 0.67 mg mL^{-1} and 70 °C is much more centralized around its peak than other distributions. Though all ***AR*** values are sampled in this distribution, the corresponding domain sizes range from 0-0.5 mm^2. This range is much narrower than for the other distributions, which instead include area measurements from 0-1 mm^2.

However, in spite of this observation, there are no strong correlations between ***AR*** and domain area in these data.

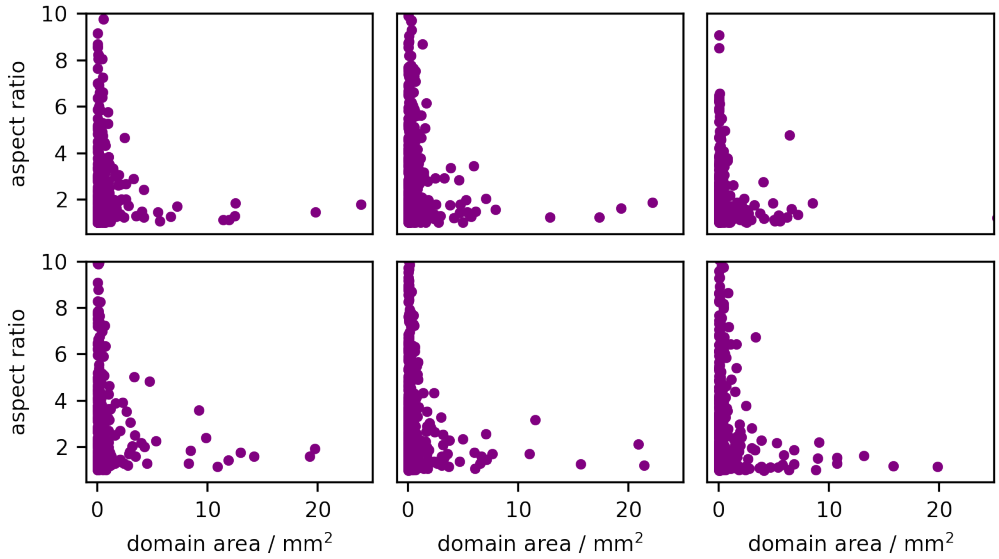

Fig. 25. ***AR*** as a function of domain area, for small domains (area < 25 mm^2) and small ***AR*** values (***AR*** ≤ 10).

Rows correspond to solution concentrations of 0.67 mg mL^{-1} (top) and 1.00 mg mL^{-1} (bottom). Columns correspond to deposition temperatures of 50, 60, and 70 °C (left to right).

The only conclusion which can be drawn from Fig. 25 is that ***AR*** values from 1-10 are equally sampled by domains smaller than 1 mm^2. This result is independent of deposition temperature and solution concentration, as shown in Fig. 25. As a consequence, there are no definitive correlations between the deposition conditions and domain ***AR*** as a function of size.

Conclusions and future work: Characterizing spatial heterogeneity in samples at structural non-equilibrium.

From the results shown in Fig. 21 through Fig. 25, it can be determined that the are no strong relationships between the deposition temperature, solution concentration, and domain metrics considered in this work. It can be concluded that all films considered exhibit a similar degree of morphological disorder. In other words, the relationship between spatial heterogeneity and environmental perturbations remains inconclusive from these data.

Potential improvements to the image analysis technique.

From the results presented in this work, we have demonstrated the utility of the homebuilt polarization-dependent brightfield microscope. Additionally, we have also presented a computational technique for quantifying the spatial morphology of TIPS-Pn films. While the data presented for the temperature- and concentration-dependent images were majorly inconclusive, this result does not diminish the value of this technique for quantification of domain metrics. Rather, these results are likely the fault of an insufficient sample size. To further improve the robustness of the temperature- and concentration-dependent results, we should consider a sample size of 10 or more films. Using only two films it is not a large enough sample size to draw meaningful conclusions about the distributions of domain metrics.

Additionally, data presented in work were collected with a microscope that was not completely aligned. The current experimental design of the microscope was changed to include a vertical bend in the light. Introducing a vertical bend (with a

mirror) increases the complexity of the alignment procedure, as any subtle deviation from perfect planarity in the incoming light is propagated more dramatically to the camera detector. By optimizing this alignment procedure, data of better quality can be collected and used in the further analysis of temperature- and concentration-effects on domain formation from solution.

Applying the image analysis technique to films at structural non-equilibrium.

Once the image analysis technique has been optimized for films of TIPS-Pn, it will be applied to examine films at structural non-equilibrium **during** formation from solution. The overall experimental microscope apparatus will remain unchanged. However, the position of the rotation stage, to which the polarizer is mounted, must be calibrated with respect to time such that the absolute polarization angle can be determined at the precise time of image acquisition.

Applying the image analysis technique to films during structural evolution should be compatible with the computational software presented in this work. One limitation to the current hardware and instrumentation is that films could no longer be stitched together during film formation. Since translating the film during formation could disrupt its aggregation pathway, only one spatial location on the film can be imaged *in situ*. As a result, the image analysis software would only be able to characterize domain formation at a single spatial location in the film.

Additionally, the current microscope design enables a 6.7 mm x 5.3 mm region of the film to be measured in one image. The size of the viewing window will inevitably limit the range of domain sizes which can be measured accurately during film formation. In this work, most domain areas were less than 10 mm^2, which is about 30%

of the viewing window. Domains of this size can be accurately resolved with the current instrumentation. However, larger domains could exceed the area of the viewing window. It follows that any domain larger than the viewing window cannot be accurately characterized by the existing image analysis software. Further consideration of this issue may be necessary if films exhibit large domains during their formation from solution.

While examining a single spatial location at once may be a limitation, the image analysis software presented in this work will still enable *in situ* measurements of mesoscopic aggregation events during film formation. This experiment would provide insight into how environmental perturbations not only affect the final domain structure in a film, but also the aggregation pathways which direct domain formation. Understanding how deposition conditions affect these aggregation mechanisms would permit further control over the physical structure and, consequently, the electronic functionality of solution-processed films of organic semiconducting molecules. Additionally, increased control over the solution-processing techniques used to develop these films would improve their reproducibility during manufacture. Better reproducibility in the production of organic semiconducting films would enable their use in a larger quantity of mainstream technological devices, including solar cells and OLEDs—technologies that are becoming increasingly widespread in our contemporary society.

References

1. He, Z., Zhang, Z. & Bi, S. Polyacrylate polymer assisted crystallization: Improved charge transport and performance consistency for solution-processable small-molecule semiconductor based organic thin film transistors. *J. Sci. Adv. Mater. Devices* **4**, 467–472 (2019).

2. He, Z., Chen, J., Sun, Z., Szulczewski, G. & Li, D. Air-flow navigated crystal growth for TIPS pentacene-based organic thin-film transistors. *Org. Electron.* **13**, 1819–1826 (2012).

3. Chen, J., Tee, C. K., Shtein, M., Anthony, J. & Martin, D. C. Grain-boundary-limited charge transport in solution-processed 6,13 bis(tri-isopropylsilylethynyl) pentacene thin film transistors. *J. Appl. Phys.* **103**, 114513 (2008).

4. He, Z. *et al.* A facile and novel route to improve TIPS pentacene based organic thin film transistor performance with elastomer. *Synth. Met.* **262**, 116337 (2020).

5. Karagiannidis, P. G., Kassavetis, S., Pitsalidis, C. & Logothetidis, S. Thermal annealing effect on the nanomechanical properties and structure of P3HT:PCBM thin films. *Thin Solid Films* **519**, 4105–4109 (2011).

6. Arunagiri, L. *et al.* Temperature-Dependent Aggregation Donor Polymers Enable Highly Efficient Sequentially Processed Organic Photovoltaics Without the Need of Orthogonal Solvents. *Adv. Funct. Mater.* **29**, 1902478 (2019).

7. Kunze, F. *et al.* Synthesis of silicon nanoparticles in a pilot-plant-scale microwave plasma reactor: Impact of flow rates and precursor concentration on the nanoparticle size and aggregation. *Powder Technol.* **342**, 880–886 (2019).

8. Krebs, F. C. Fabrication and processing of polymer solar cells: A review of printing and coating techniques. *Solar Energy Materials and Solar Cells* **93**, 394–412 (2009).

9. Kang, S. J. *et al.* Non-volatile ferroelectric poly(vinylidene fluoride-co-trifluoroethylene) memory based on a single-crystalline tri-isopropylsilylethynyl pentacene field-effect transistor. *Adv. Funct. Mater.* **19**, 1609–1616 (2009).

10. Brabec, C. J., Hauch, J. A., Schilinsky, P. & Waldauf, C. Production aspects of organic photovoltaics and their impact on the commercialization of devices. *MRS Bulletin* **30**, 50–52 (2005).

11. van Mullekom, H. A. M., Vekemans, J. A. J. M., Havinga, E. E. & Meijer, E. W. Developments in the chemistry and band gap engineering of donor–acceptor substituted conjugated polymers. *Mater. Sci. Eng. R Reports* **32**, 1–40 (2001).

12. Brédas, J. L., Calbert, J. P., Filho, D. A. da S. & Cornil, J. Organic

semiconductors: A theoretical characterization of the basic parameters governing charge transport. *Proc. Natl. Acad. Sci.* **99**, 5804–5809 (2002).

13. Jacoboni, C., Canali, C., Ottaviani, G. & Alberigi Quaranta, A. A review of some charge transport properties of silicon. *Solid. State. Electron.* **20**, 77–89 (1977).

14. van Mullekom, H., Vekemans, J. A. J. M., Havinga, E. E. & Meijer, E. W. Developments in the chemistry and band gap engineering of donor–acceptor substituted conjugated polymers. *Mater. Sci. Eng. R Reports* **32**, 1–40 (2001).

15. Turbiez, M. *et al.* Design of Organic Semiconductors: Tuning the Electronic Properties of π-Conjugated Oligothiophenes with the 3,4-Ethylenedioxythiophene (EDOT) Building Block. *Chem. - A Eur. J.* **11**, 3742–3752 (2005).

16. Muratore, C., Voevodin, A. A. & Glavin, N. R. Physical vapor deposition of 2D Van der Waals materials: a review. *Thin Solid Films* **688**, 137500 (2019).

17. Li, S. *et al.* Poly-Si/SiOx/c-Si passivating contact with 738 mV implied open circuit voltage fabricated by hot-wire chemical vapor deposition. *Appl. Phys. Lett.* **114**, 153901 (2019).

18. Wang, H., Wei, X., Du, Y. & Wang, D. Effect of water-soluble polymers on the performance of dust-suppression foams: Wettability, surface viscosity and stability. *Colloids Surfaces A Physicochem. Eng. Asp.* **568**, 92–98 (2019).

19. Petrucci, R. H., Harwood, W. S., Herring, G. E. & Madura, J. *General Chemistry: Principles and Modern Applications*. (Prentice Hall, 2007).

20. Hestand, N. J. & Spano, F. C. Molecular Aggregate Photophysics beyond the Kasha Model: Novel Design Principles for Organic Materials. *Acc. Chem. Res.* **50**, 341–350 (2017).

21. Wong, C. Y. *et al.* Revealing exciton dynamics in a small-molecule organic semiconducting film with subdomain transient absorption microscopy. *J. Phys. Chem. C* **117**, 22111–22122 (2013).

22. Delor, M., Weaver, H. L., Yu, Q. Q. & Ginsberg, N. S. Imaging material functionality through three-dimensional nanoscale tracking of energy flow. *Nat. Mater.* **19**, 56–62 (2020).

23. Sharifzadeh, S. *et al.* Relating the Physical Structure and Optoelectronic Function of Crystalline TIPS-Pentacene. *Adv. Funct. Mater.* **25**, 2038–2046 (2015).

24. Griffiths, D. J. *Introduction to Electrodynamics*. (Cambridge University Press, 2017). doi:10.1017/9781108333511

25. Jurow, M. J. *et al.* Manipulating the Transition Dipole Moment of CsPbBr 3 Perovskite Nanocrystals for Superior Optical Properties. *Nano Lett.* **19**, 2489–2496 (2019).

26. Wong, C. Y., Folie, B. D., Cotts, B. L. & Ginsberg, N. S. Discerning Variable Extents of Interdomain Orientational and Structural Heterogeneity in Solution-Cast Polycrystalline Organic Semiconducting Thin Films. *J. Phys. Chem. Lett.* **6**, 3155–3162 (2015).

27. Jiang, X. L. *et al.* Polarization dependent recordings of surface relief gratings on azobenzene containing polymer films. *Appl. Phys. Lett.* **68**, 2618–2620 (1996).

28. Chen, J., Tee, C. K., Shtein, M., Martin, D. C. & Anthony, J. Controlled solution deposition and systematic study of charge-transport anisotropy in single crystal and single-crystal textured TIPS pentacene thin films. *Org. Electron. physics, Mater. Appl.* **10**, 696–703 (2009).

29. Thorn, K. A quick guide to light microscopy in cell biology. *Mol. Biol. Cell* **27**, 219 (2016).

30. Martin, D. R., Fowlkes, C. C. & Malik, J. Learning to detect natural image boundaries using local brightness, color, and texture cues. *IEEE Trans. Pattern Anal. Mach. Intell.* **26**, 530–549 (2004).

31. Burtsev, S. V. & Kuzmin, Y. P. An efficient flood-filling algorithm. *Comput. Graph.* **17**, 549–561 (1993).

32. Codrea, M. C. & Nevalainen, O. S. Note: An algorithm for contour-based region filling. *Comput. Graph.* **29**, 441–450 (2005).